A&A, 679, A120 (2023)
https://doi.org/10.1051/0004-6361/202346869

Astronomy & Astrophysics

Gas phase Elemental abundances in Molecular cloudS (GEMS)

IX. Deuterated compounds of H_2S in starless cores

M. Rodríguez-Baras[1], G. Esplugues[1], A. Fuente[2], S. Spezzano[3], P. Caselli[3], J. C. Loison[4], E. Roueff[5], D. Navarro-Almaida[6], R. Bachiller[1], R. Martín-Doménech[2], I. Jiménez-Serra[2], L. Beitia-Antero[7], and R. Le Gal[8]

[1] Observatorio Astronómico Nacional (OAN), Alfonso XII 3, 28014 Madrid, Spain
e-mail: m.rodriguezbaras@oan.es
[2] Centro de Astrobiología (CSIC-INTA), Ctra. de Ajalvir, km 4, Torrejón de Ardoz, 28850 Madrid, Spain
[3] Centre for Astrochemical Studies, Max-Planck-Institute for Extraterrestrial Physics, Giessenbachstrasse 1, 85748 Garching, Germany
[4] Institut des Sciences Moléculaires (ISM), CNRS, Univ. Bordeaux, 351 cours de la Libération, 33400 Talence, France
[5] LERMA, Observatoire de PARIS, PSL Research University, CNRS, Sorbonne Université, 92190 Meudon, France
[6] Département d'Astrophysique (DAp), Commissariat à l'Énergie Atomique et aux Énergies Alternatives (CEA), Paris Saclay, Orme des Merisiers, Bât. 709, 91191 Gif sur Yvette, France
[7] Departamento de Estadística e Investigación Operativa, Facultad de Ciencias Matemáticas, Universidad Complutense de Madrid, Plaza de las Ciencias 3, 28040 Madrid, Spain
[8] Harvard-Smithsonian Center for Astrophysics, 60 Garden St., Cambridge, MA 02138, USA

Received 11 May 2023 / Accepted 30 August 2023

ABSTRACT

Context. H_2S is predicted to form by hydrogenation of atomic sulphur on grains and is thought to be the main sulphur reservoir in interstellar ice, being therefore a key molecule to understanding sulphur chemistry in the star formation process and to solving the missing sulphur problem in molecular clouds and star-forming regions. The study of the H_2S deuterium fraction can be used to constrain its molecule formation pathways.

Aims. The aim of this work is to investigate for the first time the deuteration of H_2S in a large sample of starless cores.

Methods. We used observations of the GEMS IRAM 30 m Large Program and complementary IRAM 30 m telescope observations. We considered a sample of 19 starless cores located in the Taurus, Perseus, and Orion molecular clouds, detecting HDS in ten of these starless cores, and D_2S in five. The single and double H_2S deuterium fractions were analysed with regard to their relation with the cloud physical parameters, comparisons with values obtained for other interstellar sources, and comparisons with deuterium fractions in early-stage star-forming sources of abundant molecules: c-C_3H_2, H_2CS, H_2O, H_2CO, and CH_3OH.

Results. We obtain a range of X(HDS)/X(H_2S) ~ 0.025−0.2 in the starless cores with HDS detections. The five starless cores with D_2S detections show values of X(D_2S)/X(HDS) ~ 0.05−0.3. H_2S single deuteration shows an inverse relation with the cloud kinetic temperature, but no trend is found with molecular hydrogen density or visual extinction. H_2S deuteration values in starless cores are similar to those observed in Class 0, although this may be a consequence of an observational bias due to the limited spatial resolution. Comparison with c-C_3H_2, H_2CS, H_2O, H_2CO, and CH_3OH in other interstellar sources reveals a general trend of decreasing deuteration with increasing temperature, with lower values for Class I and massive star-forming sources. In starless cores and Class 0 objects, H_2CS and H_2CO present higher deuteration fractions than c-C_3H_2, H_2S, H_2O, and CH_3OH. H_2O shows single and double deuteration values one order of magnitude lower than those of H_2S and CH_3OH.

Conclusions. Differences between c-C_3H_2, H_2CS and H_2CO deuterium fractions and those of H_2S, H_2O, and CH_3OH are related to deuteration processes produced in gas or solid phases, respectively. We interpret the differences between H_2S and CH_3OH deuterations and that of H_2O as a consequence of differences in the formation routes in the solid phase, which can particularly be explained in terms of the different occurrence of the D-H and H-D substitution reactions in the ice, together with the chemical desorption processes. Further interferometric observations and laboratory experiments are needed to understand the deuteration processes.

Key words. astrochemistry – ISM: abundances – ISM: molecules – ISM: clouds – stars: formation – molecular processes

1. Introduction

Stars are mainly formed in giant molecular clouds and dark cloud complexes. The cloud filamentary structure is believed to funnel interstellar gas and dust into increasingly dense concentrations, which consequently contract and fragment, leading to gravitationally bound pre-stellar cores that eventually form stars. This star formation process is regulated by different physical phenomena, such as magnetic pressure, turbulence, and rotation. Gas chemistry plays a key role: the chemical composition of the gas regulates the temperature of the gas and its ionisation fraction. Molecular emission determines the cooling of the gas, which allows the fragmentation of molecular filaments into pre-stellar cores as a consequence of diminishing the thermal support relative to self-gravity. Furthermore, the gas chemical composition determines the ionisation fraction, which controls the coupling of magnetic fields with the gas, driving the dissipation of turbulence and angular momentum transfer, and therefore playing a crucial role in the cloud collapse and the dynamics of accretion disks (Zhao et al. 2016; Padovani et al. 2013).

The chemical composition of the gas is, in turn, influenced by the star formation process itself. Therefore, the study of it in star-forming regions is a powerful diagnostic tool to determine the different processes at work and their evolution with time. Particularly interesting is the study of the deuterium fractionation, that is the process that enriches the molecules in deuterium with respect to hydrogen (Ceccarelli et al. 2014; Imai et al. 2018). The estimated cosmic deuterium abundance relative to hydrogen is $\sim 1.5 \times 10^{-5}$ (Linsky 2003), but its relative abundance in molecules is larger than this elemental D/H in very specific locations, and particularly in cold (~10 K) molecular clouds. At these temperatures, the fastest reactions are those involving ions, as most neutral-neutral reactions have activation barriers and are generally slower. H_3^+ is one of the first formed molecular ions, as a product of the cosmic ray ionisation of H_2 and H. Deuterium fractionation is mainly caused by the reaction of H_3^+ with HD, the major reservoir of D-atoms, to form H_2D^+ and H_2 (e.g. Millar et al. 1989). The formation of H_2D^+ proceeds without a reaction barrier, whereas the backward reaction with para-H_2 has an endothermicity of ~232 K (Watson 1974; Caselli & Ceccarelli 2012; Albertsson et al. 2013). In molecular clouds where the ortho-to-para ratio (OPR) of H_2 is <0.01, the H_2D^+/H_3^+ ratio becomes larger than the D/H elemental abundance for $T <$ 20−30 K (Dislaire et al. 2012). Similarly, D_2H^+ and D_3^+ are formed from H_2D^+ and D_2H^+, correspondingly, by reactions with HD. These ions react with other molecules in the gas phase, possibly donating D^+ to neutral species, enhancing their D/H ratio. The enhanced atomic D/H ratio due to the dissociative recombination of the deuterated forms of H_3^+ is transferred to grains, where it deuterates the molecules on the surface. Maximum values of the deuterium fraction are reached in dense cores ($n(H_2)>10^4$ cm^{-3}) with temperatures approximately <10−15 K, where CO molecules freeze on the grain surfaces. The molecular ion H_3^+ is efficiently destroyed by reactions with CO. When CO depletes from the gas phase, the H_3^+ abundance is enhanced and the deuterium fraction is further increased (Dalgarno & Lepp 1984; Caselli et al. 2002; Roberts et al. 2003).

High values of deuterium fraction have been found in moderately warm regions (30−70 K) such as the Orion Bar, where the H_2D^+/H_3^+ ratio is not expected to be enhanced relative to the cosmic D/H value (Parise et al. 2009). In these cases, gas-phase deuteration can occur via reactions with CH_2D^+ and C_2HD^+ (Roueff et al. 2013, 2015). At these temperatures, HD may react with CH_3^+ and $C_2H_2^+$, the reverse reactions of which have endothermicities higher than H_2D^+, leading to enhancements in the abundances of the deuterated ions CH_2D^+ and C_2HD^+ (Millar 2005). These ions react with some compounds such as HCN and H_2CO, which maintain high deuteration fractions in regions with temperatures of ~50 K (Parise et al. 2009).

The degree of deuterium fractionation is sensitive to temperature, CO depletion, H_2 density, and the OPR of H_2. Therefore, it has been extensively employed as a good tool with which to study the physical conditions and chemical states of molecular clouds (Imai et al. 2018). In general terms, the deuterium fraction is predicted to increase when the starless core evolves towards the onset of gravitational collapse, as the core density becomes more and more centrally peaked (e.g. Crapsi et al. 2007). Afterwards, the deuterium fraction drops when the young stellar object formed at the core centre begins to heat its surroundings (see e.g. Emprechtinger et al. 2009; Ceccarelli et al. 2014).

The efficiency of the deuteration enrichment in cold core conditions is now well established, with the detection of multiply deuterated molecules in starless cores and young protostars: ND_2H (Roueff et al. 2000), ND_2H and D_2CO (Loinard et al. 2001), ND_2 (Melosso et al. 2020), ND_3 (Lis et al. 2002), D_2S (Vastel et al. 2003), D_2CO (Ceccarelli et al. 2002; Bacmann et al. 2003), D_2CS (Marcelino et al. 2005), CHD_2OH, and CD_3OH (Parise et al. 2002, 2004). Despite this wealth of detections, only a few sulphur-bearing deuterated molecules (HDCS, D_2CS, HDS, and D_2S, and the molecular ion DCS^+) have been detected in dense cores and/or protostars (van Dishoeck et al. 1995; Vastel et al. 2003; Marcelino et al. 2005; Fuente et al. 2016), and in most cases the detections are restricted to a few prototypical objects. Different species probe different regions along the line of sight, and in particular S-bearing species are heavily depleted in the coldest and densest regions of starless cores (Graedel et al. 1982; Agúndez & Wakelam 2013), where N-bearing species such as NH_3, N_2H+, and nitriles (HCN, HNC, CN) are still abundant (Tafalla et al. 2006; Sipilä & Caselli 2018; Kim et al. 2020). The observation of deuterated S-bearing species therefore provides different information on the physical conditions and chemical history of starless cores.

The aim of this work is to investigate the deuteration of H_2S in cold cores. Since its first detection in W3, NGC 7538, and five other Galactic regions (Thaddeus et al. 1972), H_2S has been detected in the gas phase in several interstellar sources (e.g. Minh et al. 1989; van Dishoeck et al. 1995; Wakelam et al. 2004; Neufeld et al. 2015; Rivière-Marichalar et al. 2021). However, chemical models reveal that the observed interstellar abundance of H_2S cannot be explained by gas-phase synthesis alone. Models predict that, in the dense interstellar medium, atomic sulphur would stick on grains and be mostly hydrogenated to form H_2S (Hatchell et al. 1998; Garrod et al. 2007; Esplugues et al. 2014; Oba et al. 2019), which is thought to be the main sulphur reservoir in the ice (Vidal et al. 2017; Navarro-Almaida et al. 2020). However, H_2S has never been detected in interstellar ices and its abundance relative to water is smaller than ~1% (van Dishoeck & Blake 1998; Jiménez-Escobar & Muñoz Caro 2011). Deuterium fractionation can theoretically be used to constrain molecular formation pathways, because the ratios between the deuterated species and the main isotopologue are expected to be different if the molecule forms in the gas phase or as a result of grain surface chemistry. In the latter case, deuteration is expected to follow a statistical scheme (Brown & Millar 1989; Bacmann et al. 2020).

Gas phase Elemental abundances in Molecular CloudS (GEMS) is an IRAM 30m Large Program run between summer 2017 and 2019 that aims to measure the gas-phase elemental abundances in a set of prototypical filaments (Fuente et al. 2019; Navarro-Almaida et al. 2020; Rodríguez-Baras et al. 2021; Spezzano et al. 2022a; Esplugues et al. 2022). This work uses both GEMS and complementary IRAM 30 m observations of a wide sample of cores located in several clouds, covering different star formation activity, allowing an exploration of the role of the environment in the dynamical and chemical evolution of the pre-stellar cores. This paper presents an analysis and comparison of H_2S, HDS, and D_2S observations, which provide essential information on the formation and deuteration of this species in starless cores. The paper is structured as follows: Sect. 2 provides a summary of the observations. Section 3 presents the observational sample of starless cores and the physical properties of the corresponding star-forming regions. The derivation of physical parameters of the starless cores is described in Sect. 4. Section 5 focuses on the analysis of the measured H_2S abundances. The emission of the H_2S deuterated compounds is analysed in Sect. 6. The results obtained are discussed in Sect. 7, and our summary and conclusions are given in Sect. 8.

Table 1. Starless cores included in this work sample.

Filament	Core ID	Coordinates RA (J2000)	Dec (J2000)	Other names	Cut
		Taurus			
B 213[(1)]	#1	04:17:41.80	+28:08:47.0	5	C1
	#2	04:17:50.60	+27:56:01.0	–	C2
	#5	04:18:03.80	+28:23:06.0	7	C5
	#6	04:18:08.40	+28:05:12.0	8	C6
	#10	04:19:37.60	+27:15:31.0	13a	C10
	#12	04:19:51.70	+27:11:33.0	–	C12
	#16	04:21:21.00	+27:00:09.0	–	C16
		Perseus			
L1448[(2)]	#32	03:25:49.00	+30:42:24.6		C1
NGC 1333[(2)]	#46	03:29:11.00	+31:18:27.4	SK20[(3)]	C3-1
	#60	03:28:39.40	+31:18:27.4		C3-14
	#51	03:29:08.80	+31:15:18.1	SK16	C4
	#53	03:29:04.50	+31:20:59.1	SK26	C5
	#57	03:29:18.20	+31:25:10.8	SK33	C6
	#64	03:29:25.50	+31:28:18.1		C7
Barnard 1[(2)]	1b	03:33:20.80	+31:07:34.0		C1
Barnard 5[(2)]	#79	03:47:38.99	+32:52:15.0		C1
IC 348[(2)]	#1	03:44:01.00	+32:01:54.8		C1-1
		Orion A			
OMC-3		05:35:19.54	−05:00:41.5		C1
OMC-4		05:35:08.15	−05:35:41.5		C2

Notes. Observation cuts associated with these starless cores in GEMS observations are indicated. [(1)]B213 core IDs are from Hacar et al. (2013). IDs indicated in the "Other names" column are from Onishi et al. (2002). [(2)]Perseus core IDs (L 1448, NGC 1333, Barnard 1, Barnard 5, and IC348) are from Hatchell et al. (2007b). [(3)]NGC 1333 core IDs indicated in the "Other names" column are from Sandell & Knee (2001).

2. Observations

Part of the data employed in this work, particularly those corresponding to the emission of o-H_2S (transition $1_{10} \rightarrow 1_{01}$ at 168.763 GHz) and $H_2^{34}S$ (transition $1_{10} \rightarrow 1_{01}$ at 167.911 GHz), were observed by the GEMS Large Program. These observations are thoroughly described in Fuente et al. (2019) and only a summary is provided here. The 3 and 2 mm observations were carried out using the IRAM 30 m telescope at Pico Veleta (Spain). The observing mode was frequency switching, with a frequency throw of 6 MHz. The Eight MIxer Receivers (EMIR) and the fast Fourier transform spectrometers (FTS), with a spectral resolution of 49 kHz (∼0.09 km s^{-1}), were used.

This work also uses specific observations of the selected sources (described in Sect. 3) focused on the emission of the H_2S deuterated compounds: HDS (transition $1_{01} \rightarrow 0_{00}$ at 244.555 GHz, with E_u = 11.7 K) and o-D_2S (transition $1_{11} \rightarrow 0_{00}$ at 237.904 GHz, with E_u = 11.4 K). These are the lowest-lying transitions for the two molecules. These 1 mm observations were carried out with the IRAM 30 m telescope between 8 and 14 September 2021, using EMIR and FTS, with a spectral resolution of 200 kHz (∼0.24 km s^{-1}). The observing mode was frequency switching, with a frequency throw of 12 MHz, adapted to remove standing waves between the secondary mirror and the receivers.

The intensity scale is $T_{\rm MB}$, which is related with T_A^* by $T_{\rm MB} = (F_{\rm eff}/B_{\rm eff})T_A^*$, where $F_{\rm eff}$ is the telescope forward efficiency and $B_{\rm eff}$ is the main beam efficiency[1]. For the IRAM 30 m telescope, the difference between the T_A^* and $T_{\rm MB}$ scales is ∼27% at 145 GHz and ∼56% at 230 GHz. The half-power beam widths (HPBW) are 16 arcsec and 10.7 arcsec at 145 GHz and 230 GHz, respectively. The data reduction was carried out using GILDAS[2]/CLASS, following a standard procedure. The line intensity errors, considering calibration, size, source, and other factors, are assumed to be ∼20%, with the exception of two D_2S lines (sources B213-C1-1 and L1448-1), where the associated uncertainty is 25%.

3. Observational sample

The observational sample of this work is composed of 19 starless cores that are a subset of those included in the sample of the GEMS program. The list of selected sources is shown in Table 1. The observed starless cores belong to different filaments of three nearby star-forming regions: Taurus, Perseus, and Orion. These molecular cloud complexes are characterised by having different star formation activity and therefore different illumination. The comparison of starless cores located in the same filament allows the investigation of the effect of time evolution on the chemistry of dark cores (see e.g. Frau et al. 2012). The comparison of starless cores in different star-forming regions provides information about the influence of UV radiation on the gas composition, and the general effect of the environment on the chemistry of the cores. The characteristics of the selected regions are thoroughly described in Rodríguez-Baras et al. (2021). As a summary, the main properties of the considered filaments are the following:

Taurus: B213/L1495. The Taurus molecular cloud is located at a distance of 145 pc (Yan et al. 2019). With a total mass of 1.5×10^4 $M_\odot$ derived from CO data (Pineda et al. 2010),

[1] https://publicwiki.iram.es/Iram30mEfficiencies

[2] https://www.iram.fr/IRAMFR/GILDAS/

it is known to contain more than 250 young stellar objects. It is considered an archetype of exclusively low-mass star-forming regions. It has been the target of several cloud evolution and star formation studies (Ungerechts & Thaddeus 1987; Mizuno et al. 1995; Goldsmith et al. 2008), being extensively mapped in CO (Cernicharo & Guelin 1987; Onishi et al. 1996; Narayanan et al. 2008) and visual extinction (Cambrésy 1999; Padoan et al. 2002; Schmalzl et al. 2010).

B213/L1495 is a Taurus prominent filament, a clear example of a star-forming region where the magnetic field lines are perpendicular to the main filament (Soler 2019). The morphology of the map, with striations perpendicular to the filament, suggests that the filament is accreting material from its surroundings (Goldsmith et al. 2008; Palmeirim et al. 2013). A population of dense cores are embedded in this filament (Benson & Myers 1989; Onishi et al. 2002; Tatematsu et al. 2004; Hacar et al. 2013; Punanova et al. 2018). Some of these dense cores are starless, while others are associated with young stellar objects (YSOs) of different ages. Interestingly, the density of stars decreases from north to south suggesting a different dynamical or chemical age along the filament. GEMS observed nine cuts along clumps #1, # 2, #5, #6, #7, #10, #12, #16, and #17 (core numbers from the catalogue of Hacar et al. 2013). All these cores except #7 and #17 were observed in the deuterated compounds of H_2S, and are therefore included in this work. We use the H_2 column density and dust temperature maps of B213 obtained by Palmeirim et al. (2013) on the basis of the *Herschel* Gould Belt survey (André et al. 2010) and *Planck* data (c.f. Bernard et al. 2010) at an angular resolution of 18.2″.

Perseus: Barnard 1, NGC 1333, IC348, L1448, and B5. The Perseus molecular cloud is a well-known star-forming cloud, located at a distance ranging from 234 to 331 pc according to recent *Gaia* parallaxes and photometric data (Zucker et al. 2020). Perseus is the prototype of an intermediate-mass star-forming region, where the infrared survey of Ladd et al. (1993) suggested intermediate properties between Taurus, with stars predominantly forming in relative isolation (YSO surface density ∼10 pc^{-2}), and the Orion complex, with large star-forming clusters with YSO surface densities of 100 pc^{-2}. The molecular cloud complex is associated with three clusters containing pre-main-sequence stars: IC 348, with an estimated age of 2 Myr (Luhman et al. 2003); NGC 1333, which is younger than 1Myr in age (Lada et al. 1996; Wilking et al. 2004); and the Per 0B2 association, which contains a B0.5 star (Steenbrugge et al. 2003). The molecular cloud itself contains numerous protostars and dense cores (Hatchell et al. 2005, 2007a,b). GEMS observed 11 cuts along starless cores distributed in Barnard 1, IC348, L1448, NGC 1333, and B5. Those selected for this work are shown in Table 1. The group of cores in IC348 and NGC 1333 is close to the clusters and therefore immersed in a harsh environment, while Barnard 1 and L1448 are located in a quiescent region. The dust opacity and dust temperatures maps reported by Zari et al. (2016) were used in our analysis. In order to derive the molecular hydrogen column density from the dust opacity at 850 μm (τ_{850}), we used expression (7) of Zari et al. (2016) and $A_V = A_K/0.112$. This expression gives accurate values for low extinctions ($A_V < 10$ mag) but may underestimate their value towards the extinction peaks. In the range of values considered in Perseus, A_V ∼3−30 mag, the uncertainty in the values of A_V is a factor of two.

Orion A. The Orion molecular cloud, at a distance of ∼428 pc (Zucker et al. 2019), is the most massive and most active star-forming complex in the local neighborhood. It is a large complex, composed itself of two giant molecular clouds: Orion A, hosting the HII region usually called the Orion nebula, and the more quiescent Orion B (see, e.g., Pety et al. 2017). Different clouds have been identified within Orion A based on millimeter, submillimeter, and infrared observations. Orion molecular cloud 1 (OMC 1) was identified as dense gas directly associated with Orion KL (Wilson et al. 1970; Zuckerman 1973; Liszt et al. 1974), then OMC 2 (Gatley et al. 1974) and OMC 3 (Kutner et al. 1976) were detected as subsequent clumps in the CO emission located about 15′ and 25′ to the north of OMC 1. Bally et al. (1987) revealed that these clouds consist of the integral-shaped filament (ISF) of molecular gas, part itself of a larger filamentary structure extending from north to south over 4°. OMC 4 (Johnstone & Bally 1999) and OMC 5 (Johnstone & Bally 2006) are concentrations of submillimeter continuum emission in the southern part of the ISF. GEMS observed three cuts along OMC-2 (ORI-C3), OMC-3 (ORI-C1), and OMC-4 (ORI-C2). These cuts avoid the protostars and stars in this active star-forming region, probing different environments because of their different distance from the Orion nebula. In this work we consider the visual extinction peaks along cuts ORI-C1 and ORI-C2, while cut ORI-C3 was not observed in the deuterated compounds of H_2S. In our analysis, we used the dust opacity and dust temperatures maps reported by Lombardi et al. (2014). The values of the molecular hydrogen column density were derived from the dust opacity at 850 μm, using expression $A_K = 2640 \times \tau_{850} + 0.012$ of Lombardi et al. (2014) and $A_V = A_K/0.112$.

4. Physical parameters of the starless cores

The star-forming regions Taurus, Perseus, and Orion were observed with *Herschel* and SCUBA as part of the Gould Belt survey (André et al. 2010), and accurate visual extinction (A_V) and dust temperature (T_d) maps are available (Malinen et al. 2012; Hatchell et al. 2005; Lombardi et al. 2014; Zari et al. 2016). The angular resolution of the A_V-T_d maps (∼36″) is similar to that provided by the 30 m telescope at 3 mm, allowing a direct comparison of continuum and spectroscopic data. Throughout this paper we adopt the relation between visual extinction and molecular hydrogen column density $A_V \approx N(H_2) \times 10^{-21}$ mag (Bohlin et al. 1978).

We adopted the molecular hydrogen densities, $n(H_2)$, obtained by Rodríguez-Baras et al. (2021) towards the selected positions. In that paper we used the line intensities of the observed CS, $C^{34}S$, and ^{13}CS lines to estimate $n(H_2)$ at each of the GEMS positions. CS has been largely used as a density and column density tracer in the interstellar medium (e.g. Linke & Goldsmith 1980; Anglada et al. 1996; Shirley et al. 2003; Wu et al. 2010; Zhang et al. 2014; Scourfield et al. 2020) The lines were fitted using the non-LTE molecular excitation and radiative transfer code RADEX (van der Tak et al. 2007) and the collisional coefficients calculated by Denis-Alpizar et al. (2018). In addition, they assumed that gas and dust are thermalised, in other words the kinetic temperature, T_k, is equal to the dust temperature derived from far infrared and millimeter observations (TMC 1: Fuente et al. 2019; B 213: Palmeirim et al. 2013; Perseus: Zari et al. 2016; Orion: Lombardi et al. 2014). Furthermore, the beam filling factor was assumed to be ∼1 towards all positions, so we considered the emission to be extended compared to the IRAM 30 m beam size at the observed frequencies, which is a reasonable assumption according to our CS data (see Fuente et al. 2019; Navarro-Almaida et al. 2020; Rodríguez-Baras et al. 2021). In the calculations we let $n(H_2)$

Table 2. Line parameters from Gaussian fits.

Starless core	H_2S $1_{10} \rightarrow 1_{01}$			$H_2^{34}S$ $1_{10} \rightarrow 1_{01}$			HDS $1_{01} \rightarrow 0_{00}$			D_2S $1_{11} \rightarrow 0_{00}$		
	V_{LSR} (km s^{-1})	$\triangle V$ (km s^{-1})	T_{MB} (K)	V_{LSR} (km s^{-1})	$\triangle V$ (km s^{-1})	T_{MB} (K)	V_{LSR} (km s^{-1})	$\triangle V$ (km s^{-1})	T_{MB} (K)	V_{LSR} (km s^{-1})	$\triangle V$ (km s^{-1})	T_{MB} (K)
B213-C1-1	5.87 ± 0.01	0.68 ± 0.02	0.49 ± 0.10	5.99 ± 0.02	0.35 ± 0.04	0.11 ± 0.02	5.95 ± 0.01	0.57 ± 0.04	0.18 ± 0.04	5.99 ± 0.07	0.57 ± 0.14	0.03 ± 0.01
B213-C2-1	7.08 ± 0.01	0.30 ± 0.02	0.20 ± 0.04	7.06 ± 0.02	0.13 ± 0.05	0.04 ± 0.01	7.03 ± 0.04	0.49 ± 0.09	0.07 ± 0.01			<0.05
B213-C5-1	6.51 ± 0.01	0.66 ± 0.03	0.35 ± 0.07						<0.05			<0.05
B213-C6-1	6.87 ± 0.01	0.83 ± 0.02	0.30 ± 0.06				7.06 ± 0.02	0.41 ± 0.05	0.09 ± 0.02			<0.03
B213-C10-1	6.85 ± 0.02	0.29 ± 0.05	0.22 ± 0.04						<0.11			<0.07
B213-C12-1	6.81 ± 0.02	0.31 ± 0.03	0.24 ± 0.05						<0.08			<0.08
B213-C16-1	6.75 ± 0.05	0.76 ± 0.09	0.08 ± 0.02						<0.04			<0.04
IC348-1	8.96 ± 0.01	0.81 ± 0.02	0.98 ± 0.20						<0.06			<0.04
L1448-1	4.64 ± 0.01	0.73 ± 0.03	0.65 ± 0.13	4.43 ± 0.03	0.32 ± 0.06	0.15 ± 0.03	4.59 ± 0.01	0.50 ± 0.02	0.32 ± 0.06	4.74 ± 0.07	0.51 ± 0.17	0.03 ± 0.01
1333-C3-1	8.55 ± 0.01	1.22 ± 0.02	1.28 ± 0.26				8.78 ± 0.04	0.69 ± 0.11	0.07 ± 0.01			<0.03
1333-C4-1	7.65 ± 0.01	1.45 ± 0.01	2.27 ± 0.45	7.63 ± 0.02	1.03 ± 0.04	0.40 ± 0.08	7.72 ± 0.01	1.12 ± 0.01	0.80 ± 0.16	7.92 ± 0.03	1.14 ± 0.06	0.15 ± 0.03
1333-C5-1	7.64 ± 0.01	1.01 ± 0.02	1.12 ± 0.22						<0.06			<0.06
1333-C6-1	7.50 ± 0.01	0.45 ± 0.01	1.49 ± 0.30						<0.09			<0.08
1333-C7-1	7.64 ± 0.01	0.64 ± 0.02	0.80 ± 0.16				7.66 ± 0.03	0.62 ± 0.06	0.12 ± 0.02			<0.05
1333-C3-14	7.91 ± 0.01	0.64 ± 0.01	1.32 ± 0.26	7.96 ± 0.04	0.48 ± 0.08	0.15 ± 0.03	8.11 ± 0.01	0.74 ± 0.03	0.24 ± 0.05			<0.03
79-C1-1	10.44 ± 0.01	0.67 ± 0.03	0.45 ± 0.09	10.55 ± 0.03	0.32 ± 0.08	0.06 ± 0.01	10.39 ± 0.02	0.63 ± 0.03	0.22 ± 0.04	10.49 ± 0.04	0.58 ± 0.08	0.09 ± 0.02
Ori-C2-3	8.05 ± 0.02	1.32 ± 0.04	0.73 ± 0.15	8.11 ± 0.05	0.33 ± 0.08	0.09 ± 0.02			<0.04			<0.04
Ori-C1-2	10.96 ± 0.01	1.59 ± 0.01	2.10 ± 0.42	11.00 ± 0.03	1.00 ± 0.07	0.19 ± 0.04			<0.04			<0.03
B1b-Cal	6.49 ± 0.01	1.11 ± 0.02	1.35 ± 0.27	6.63 ± 0.01	0.73 ± 0.03	0.36 ± 0.07	6.55 ± 0.01	0.88 ± 0.02	0.57 ± 0.11	6.68 ± 0.03	1.01 ± 0.10	0.11 ± 0.02

Notes. In the case of HDS and D_2S non-detections, the upper limit of the line intensity is estimated as three times the rms in temperature. The line area upper limit is obtained by multiplying the intensity upper limit by the width of the H_2S line measured in that spectrum.

and N(CS) vary as free parameters and explored their parameter space following the Monte Carlo Markov chain (MCMC) methodology with a Bayesian inference approach. In particular, we used the "emcee" (Foreman-Mackey et al. 2013) implementation of the invariant MCMC ensemble sampler methods by Goodman & Weare (2010). This method was already used in Rivière-Marichalar et al. (2019) and Navarro-Almaida et al. (2020), and allowed us to estimate the molecular hydrogen density as long as the two transitions of CS, J = 2→1 and 3→2, were detected, which was the case with all the starless cores considered in this work sample. The complete procedure, and the caveats that had to be taken into account, are described in detail in Rodríguez-Baras et al. (2021).

5. The H_2S abundance

Sulphur atoms in interstellar ice mantles are expected to preferentially form H_2S because of the high hydrogen abundances and the mobility of hydrogen in the ice matrix. Studying H_2S abundance in the gas phase is essential to our understanding of the chemical processes that lead to sulphur depletion in these environments. In order to derive accurate H_2S column densities, avoiding possible opacity effects, we have observed the o-H_2S $1_{10} \rightarrow 1_{01}$ and o-$H_2^{34}S$ $1_{10} \rightarrow 1_{01}$ lines. The o-H_2S line emission has been detected in the whole sample, while its isotopologue, o-$H_2^{34}S$, has only been detected in ten out of the 24 sources (three in Taurus, five in Perseus, and two in Orion). The line parameters from the line Gaussian fits are shown in Table 2. We determined the molecular column densities of o-H_2S and o-$H_2^{34}S$ using the RADEX code, the volume densities obtained by Rodríguez-Baras et al. (2021), and the collisional coefficients calculated by Dagdigian (2020). The obtained column densities are included in Table 3. Uncertainties are considered to be 20%, consistent with errors associated with the line measurements, and estimated by propagation in quadrature in any calculation provided.

Figure 1 presents the relationship between the o-H_2S and o-$H_2^{34}S$ column density ratio and the main physical parameters of the starless cores (kinetic temperature, extinction, and molecular hydrogen density). A clear direct relation with temperature can be observed (with a Pearson correlation coefficient of 0.91), where the standard isotopic value expected for the $H_2S/H_2^{34}S$ ratio (22.5, Gratier et al. 2016) is only reached at the highest temperatures observed in our starless cores. This apparent correlation is the result of the fact that the H_2S $1_{10} \rightarrow 1_{01}$ line is optically thick in the dense environments we are considering. In this regime, the fitting to the o-H_2S line only provides a lower limit to its column density, and therefore to the $H_2S/H_2^{34}S$ ratio. To avoid these opacity effects in the analysis of the o-H_2S emission and related quantities, in those starless cores where o-$H_2^{34}S$ emission is detected we estimated the o-H_2S column density by scaling the o-$H_2^{34}S$ column density using the 22.5 standard ratio (Gratier et al. 2016). A proper distinction was made between both cases, and it should be taken into account that, when directly measured o-H_2S is considered, these column densities and corresponding abundances could be underestimated.

In the case of molecules formed on the ice surface, the OPR might differ from the thermal equilibrium value. Indeed, laboratory experiments reported by Hama et al. (2018) show that the OPR of desorbed H_2O molecules is close to the statistical value of three even at very low temperatures. This would be the case for H_2S molecules that mainly form on grain surfaces as long as subsequent gas-phase chemistry has no time to change it. Sipilä et al. (2015) modeled the spin-state chemistry of H_2O in starless cores and found that at late times (~10^6 yr) the OPR would be ~1.6. We determined the H_2S abundances adopting OPR = 3. The thermal equilibrium value of the OPR of H_2S is ~1.8 at ~12 K. Therefore, we consider that the uncertainty due to the assumed OPR is less than a factor of 1.7. The relations between the obtained o-H_2S abundances and the physical parameters of the starless cores are shown in Fig. 2. This figure can be directly compared with Fig. 14 by Rodríguez-Baras et al. (2021), where analog relations are presented for the complete GEMS observations. The trends and distributions obtained in this case for the starless cores confirm those observed in the mentioned reference. Under the physical conditions prevailing in dark clouds, the main driver of the H_2S abundance behaviour seems to be the molecular hydrogen abundance, where a strong anti-correlation is

Table 3. Starless cores' physical properties, measured column densities of the studied compounds, and estimated H_2S, HDS, and D_2S abundances.

Starless core	T_{kin} (K)	A_V (mag)	$n(H_2)$ (cm^{-3})	o-H_2S[(1)] (cm^{-2})	o-$H_2^{34}S$ (cm^{-2})	HDS (cm^{-2})	o-D_2S (cm^{-2})	X(H_2S)[(2)]	X(HDS)	X(D_2S)
					Taurus					
B213-C1-1	10.9	26.9	1.23×10^4 (8.83×10^3)	1.14×10^{14} (2.58×10^{12})	1.55×10^{13} (3.10×10^{12})	3.25×10^{13} (6.49×10^{12})	1.60×10^{12} (3.68×10^{11})	1.73×10^{-08} (3.45×10^{-09})	1.21×10^{-09} (2.41×10^{-10})	8.94×10^{-11} (2.05×10^{-11})
B213-C2-1	11	20.9	2.79×10^4 (2.64×10^4)	6.65×10^{12} (6.14×10^{11})	8.17×10^{11} (1.63×10^{11})	3.90×10^{12} (7.80×10^{11})	$<1.33 \times 10^{12}$	1.17×10^{-09} (2.34×10^{-10})	1.87×10^{-10} (3.73×10^{-11})	$<9.57 \times 10^{-11}$
B213-C5-1	11.9	23.6	4.68×10^4 (3.29×10^4)	1.49×10^{13} (6.70×10^{11})		$<2.10 \times 10^{12}$	$<1.63 \times 10^{12}$	8.43×10^{-10} (3.78×10^{-11})	$<8.88 \times 10^{-11}$	$<1.04 \times 10^{-10}$
B213-C6-1	10.9	22.2	8.28×10^4 (8.05×10^4)	1.02×10^{13} (3.07×10^{11})		1.98×10^{12} (3.95×10^{11})	$<7.81 \times 10^{11}$	6.10×10^{-10} (1.84×10^{-11})	8.90×10^{-11} (1.78×10^{-11})	$<5.28 \times 10^{-11}$
B213-C10-1	11.2	20.7	4.32×10^4 (5.09×10^4)	4.37×10^{12} (5.87×10^{11})		$<2.73 \times 10^{12}$	$<1.19 \times 10^{12}$	2.82×10^{-10} (3.78×10^{-11})	$<1.32 \times 10^{-10}$	$<8.59 \times 10^{-11}$
B213-C12-1	10.6	22.1	1.43×10^5 (1.40×10^5)	2.00×10^{12} (2.25×10^{11})		$<9.32 \times 10^{11}$	$<5.23 \times 10^{11}$	1.21×10^{-10} (1.36×10^{-11})	$<4.22 \times 10^{-11}$	$<3.55 \times 10^{-11}$
B213-C16-1	10.3	24.8	2.07×10^4 (1.83×10^4)	8.57×10^{12} (1.07×10^{12})		$<4.46 \times 10^{12}$	$<3.51 \times 10^{12}$	4.61×10^{-10} (5.76×10^{-11})	$<1.80 \times 10^{-10}$	$<2.13 \times 10^{-10}$
					Perseus					
IC348-C1-1	21.7	21.8	4.49×10^4 (2.54×10^4)	4.29×10^{13} (8.19×10^{11})		$<2.24 \times 10^{12}$	$<8.49 \times 10^{11}$	2.62×10^{-09} (5.01×10^{-11})	$<1.03 \times 10^{-10}$	$<5.84 \times 10^{-11}$
L1448-C1	15.1	28.4	1.01×10^4 (7.08×10^3)	1.51×10^{14} (4.54×10^{12})	1.98×10^{13} (3.96×10^{12})	4.88×10^{13} (9.76×10^{12})	2.29×10^{12} (5.55×10^{11})	2.09×10^{-08} ($4.18 \times t10^{-09}$)	1.72×10^{-09} (3.44×10^{-10})	1.21×10^{-10} (2.93×10^{-11})
1333-C3-1	17.7	30.3	9.34×10^4 (4.35×10^4)	5.18×10^{13} (6.28×10^{11})		1.71×10^{12} (3.42×10^{11})	$<5.41 \times 10^{11}$	2.28×10^{-09} (2.76×10^{-11})	5.65×10^{-11} (1.13×10^{-11})	$<2.68 \times 10^{-11}$
1333-C3-14	15.9	26.8	1.04×10^4 (6.44×10^3)	3.18×10^{14} (4.63×10^{12})	2.82×10^{13} (5.63×10^{12})	4.47×10^{13} (8.94×10^{12})	$<2.62 \times 10^{12}$	3.15×10^{-08} (6.31×10^{-09})	1.68×10^{-09} (3.33×10^{-10})	$<1.46 \times 10^{-10}$
1333-C4-1	16.8	39.9	5.76×10^4 (3.70×10^4)	2.72×10^{14} (1.87×10^{12})	2.90×10^{13} (5.79×10^{12})	5.49×10^{13} (1.10×10^{13})	4.49×10^{12} (8.97×10^{11})	2.18×10^{-08} (4.36×10^{-09})	1.38×10^{-09} (2.75×10^{-10})	1.69×10^{-10} (3.37×10^{-11})
1333-C5-1	19.2	27.5	8.65×10^4 (4.90×10^4)	3.63×10^{13} (6.08×10^{11})		$<2.02 \times 10^{12}$	$<8.97 \times 10^{11}$	1.76×10^{-09} (2.95×10^{-11})	$<7.34 \times 10^{-11}$	$<4.89 \times 10^{-11}$
1333-C6-1	19.9	16.1	4.74×10^4 (3.18×10^4)	4.53×10^{13} (1.89×10^{12})		$<1.92 \times 10^{12}$	$<8.94 \times 10^{11}$	3.75×10^{-09} (1.56×10^{-10})	$<1.19 \times 10^{-10}$	$<8.33 \times 10^{-11}$
1333-C7-1	17.3	17.6	1.35×10^5 (8.90×10^4)	1.13×10^{13} (3.09×10^{11})		2.20×10^{12} (4.39×10^{11})	$<4.11 \times 10^{11}$	8.56×10^{-10} (2.34×10^{-11})	1.25×10^{-10} (2.50×10^{-11})	$<3.50 \times 10^{-11}$
79-C1-1	15.4	19.9	1.93×10^4 (1.86×10^4)	4.09×10^{13} (4.63×10^{12})	3.71×10^{12} (5.63×10^{12})	1.89×10^{13} (8.94×10^{12})	4.19×10^{12} (2.62×10^{12})	5.59×10^{-09} (1.13×10^{-10})	9.50×10^{-10} (1.90×10^{-10})	3.16×10^{-10} (6.32×10^{-11})
B1b	11.9	76.0	3.15×10^5 (3.00×10^5)	2.69×10^{13} (3.75×10^{11})	5.20×10^{12} (1.04×10^{12})	1.40×10^{13} (2.80×10^{12})	1.20×10^{12} (2.41×10^{11})	2.05×10^{-09} (4.11×10^{-10})	1.84×10^{-10} (3.68×10^{-11})	2.37×10^{-11} (4.75×10^{-12})
					Orion					
ORI-C1-2	18.1	173	3.43×10^4 (1.95×10^4)	4.28×10^{14} (2.18×10^{12})	2.75×10^{13} (5.50×10^{12})	$<3.74 \times 10^{12}$	$<1.49 \times 10^{12}$	4.77×10^{-09} (9.54×10^{-10})	$<2.16 \times 10^{-11}$	$<1.30 \times 10^{-11}$
ORI-C2-3	22.8	56.5	2.61×10^4 (1.72×10^4)	8.09×10^{13} (3.20×10^{12})	3.38×10^{12} (6.77×10^{11})	$<3.64 \times 10^{12}$	$<1.80 \times 10^{12}$	1.80×10^{-09} (3.59×10^{-10})	$<6.44 \times 10^{-11}$	$<4.77 \times 10^{-11}$

Notes. Uncertainties are provided within parentheses. [(1)]Determination was made with direct line measures. [(2)]The abundance was estimated by scaling the o-$H_2^{34}S$ column density using the 22.5 standard ratio (Gratier et al. 2016) in those cases where the isotopologue was available, or by direct determination of the o-H_2S column density when the isotopologue was not available. An OPR of three was adopted for H_2S, and of two for D_2S.

observed. Rodríguez-Baras et al. (2021) already considered that optical depth effects were not expected to bias the observed anti-correlation with $n(H_2)$, and this is confirmed by the same trend shown by starless cores where the H_2S abundance is derived from $H_2^{34}S$ detections. Particularly high values of the H_2S abundance in a few starless cores could be due to the strong influence of the star formation activity in their surroundings: this is the case, for example, with B213-C1-1, located towards the northern region of Taurus, which has a higher stellar formation activity and thus the possible influence of outflows, or with 1333-C3-14, in Perseus, classified as a protostar. Non-thermal desorption of H_2S driven by the enhanced cosmic-ray flux and shocks associated with bipolar outflows are most likely the cause of this behaviour.

6. Deuterated compounds: HDS and D_2S

One of the options for addressing the unsolved questions about H_2S formation and evolution, and sulphur chemistry in general, is the study of its deuterium fraction through the analysis of the emission of its first deuterated compound, HDS, and its second deuterated compound, D_2S. HDS was first observed by

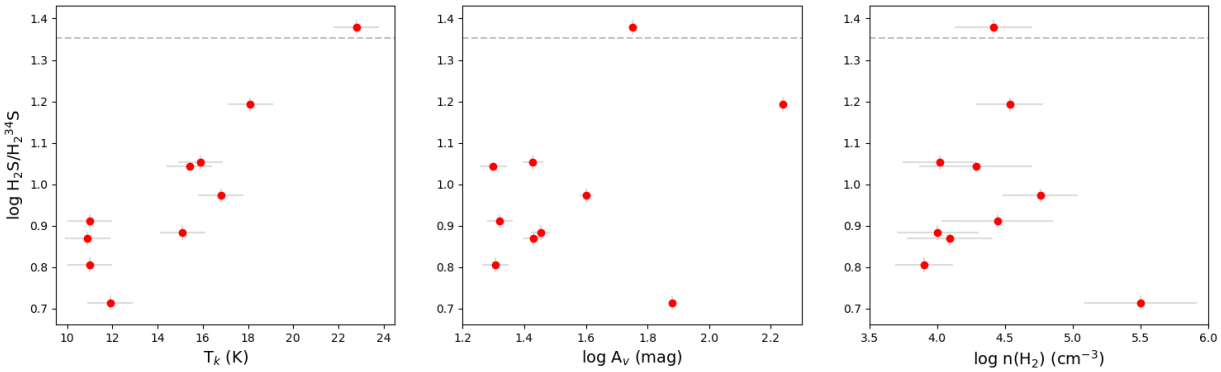

Fig. 1. Relation of the $H_2S/H_2^{34}S$ column density ratio to cloud physical parameters: kinetic temperature (left), extinction (middle), and molecular hydrogen density (right). The dashed grey line indicates the standard isotopic value expected for the $H_2S/H_2^{34}S$ ratio (22.5, Gratier et al. 2016).

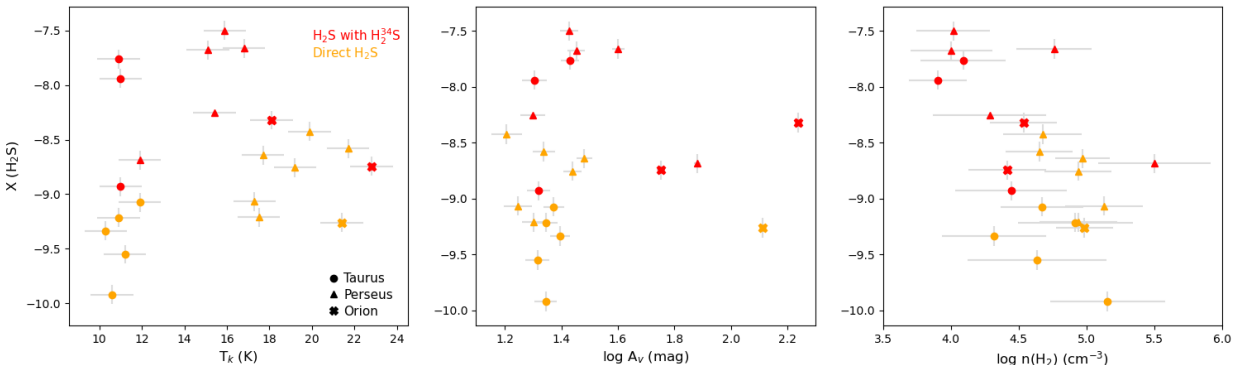

Fig. 2. Relation of the H_2S molecular abundance to cloud physical parameters: kinetic temperature (left), extinction (middle), and molecular hydrogen density (right). The dataset is colour-coded according to the method applied for the estimation of the abundance, and the symbol shape indicates the molecular cloud of the points, as shown in the legends.

van Dishoeck et al. (1995) towards the cold star-forming core IRAS 16293, and since then some upper limits have been measured in several hot cores (Hatchell et al. 1999; Crockett et al. 2014). The first detection of D_2S was made by Vastel et al. (2003) in NGC 1333 IRAS 4A and B1b, with some upper limits measured in a wider sample of Class 0 sources and dense cores.

We detect HDS emission in ten of our starless cores and D_2S in five. In the case of the Taurus cloud, HDS is detected in three starless cores (B213-C1-1, B213-C2-1, and B213-C6-1), while D_2S is only located in one (B213-C1-1). These three cores are located in the northern zone of the filament, which is characterised by a higher star formation activity compared to the southern part (Hacar et al. 2013). High deuteration fractions of H_2CS have also been measured in these northern cores by Esplugues et al. (2022). Regarding Perseus, HDS is detected in seven starless cores (L1448-1, 1333-C3-1, 1333-C4-1, 1333-c7-1, 1333-C3-14, 79-C1-1, and B1b) and D_2S is detected in four (L1448-1, 1333-C4-1, 79-C1-1, and B1b). IC348 is the only Perseus filament where no deuterated H_2S is detected, probably due to the fact that it is located in a warmer environment (Knee & Sandell 2000; Plunkett et al. 2013). There is no detection of HDS or D_2S in the Orion starless cores.

HDS and o-D_2S line parameters from Gaussian fits are included in Table 2, as well as the intensity upper limits in the case of non-detections. Column densities are derived following the same method explained in Sect. 5, using the RADEX code and HDS and o-D_2S collisional coefficients by Dagdigian (2022). Obtained values are included in Table 3. Upper limits are derived for those sources where the corresponding emission is not detected. Abundances are estimated for both HDS and D_2S, considering in the case of o-D_2S an OPR of two, and are also included in Table 3.

6.1. Relation with cloud physical parameters

The relations between HDS/H_2S, D_2S/H_2S, and D_2S/HDS abundance ratios to starless cores' physical parameters are represented in Fig. 3. Distinctions are made between the corresponding molecular clouds, the method applied for the derivation of the H_2S abundance, and starless cores with direct measurements or estimated upper limits of HDS or D_2S, as indicated. In the case of the D_2S/HDS ratio, only sources with direct measurements of both compounds or at least direct measurement of HDS are represented, as the cases with both upper limits introduced an excess of degeneracy.

Regarding the clouds, single deuteration values (i.e. HDS/H_2S abundance ratios) seem to be slightly higher in Taurus than in Perseus, although this should be considered with caution since several Taurus values are at the upper limits. One of the Orion starless cores, Ori-C1-2, shows an upper limit of the HDS/H_2S ratio lower than the other, with a value more than one order of magnitude lower than those measured in Taurus and Perseus. However, we cannot extrapolate this behaviour to the starless cores located in Orion A. Esplugues et al. (2022) finds large differences, of about one order of magnitude, in the deuterium fractions of H_2CS towards the starless cores located in Orion.

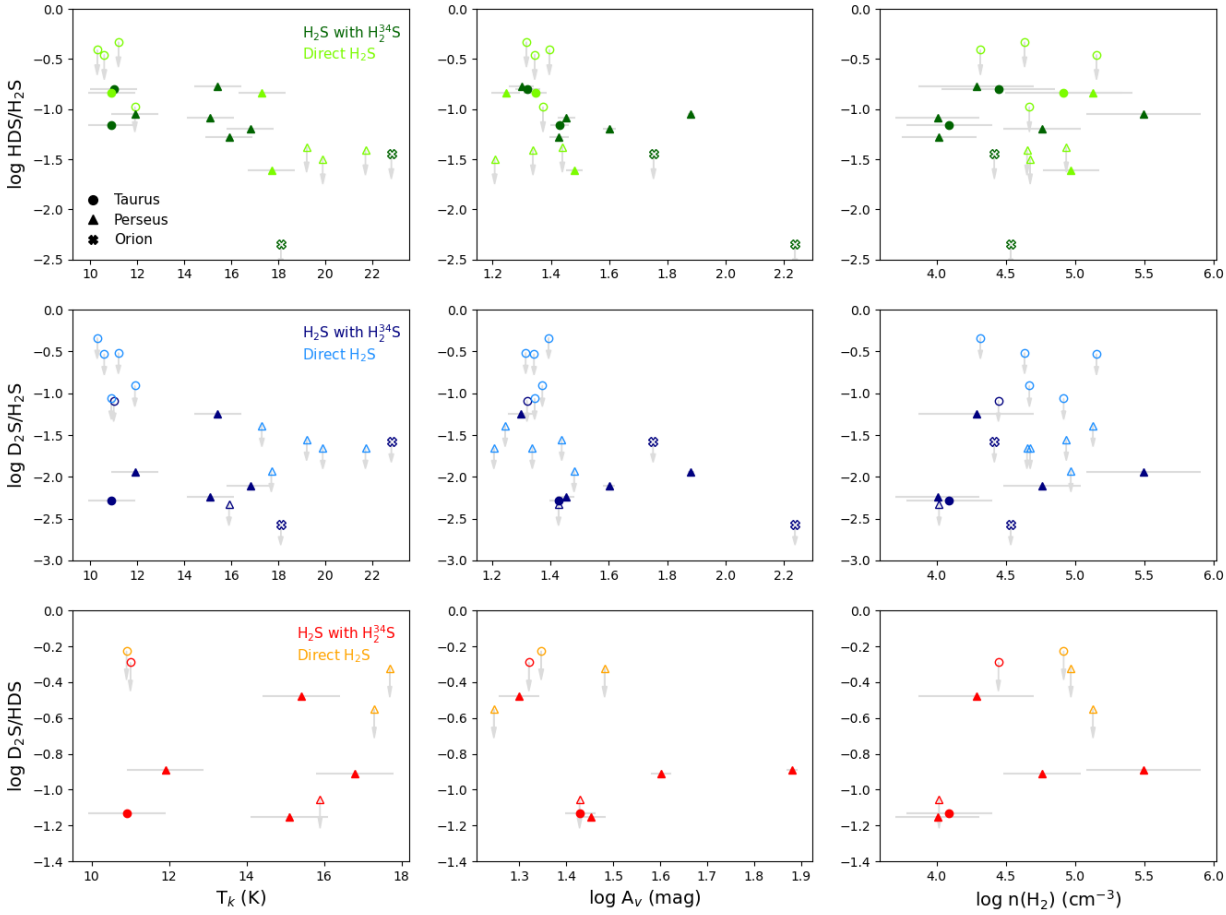

Fig. 3. Relation between HDS/H_2S (top row), D_2S/H_2S (middle row), and D_2S/HDS (bottom row) abundance ratios and starless cores' physical parameters: kinetic temperature (left), extinction (middle), and molecular hydrogen density (right). The dataset is colour-coded in each row according to the way of estimation of H_2S column density, as indicated in the legends. Different symbols indicate the molecular cloud of the points, as indicated in the legend of the first panel. Filled symbols correspond to direct detections of HDS (top row) or D_2S (middle row), and open symbols correspond to the upper limits, respectively. In the case of D_2S/HDS (bottom row), filled symbols indicate direct detection of both HDS and D_2S, and open symbols indicate the direct detection of HDS and the upper limits of D_2S.

All in all, a decreasing relation between H_2S single deuteration and kinetic temperature is observed for the whole sample. This decreasing relation is expected, since low temperatures favour higher values of the D/H ratio. In particular, we do not have any detections in positions with $T > 18$ K, which confirms that CO depletion is an important parameter for deuteration. The HDS/H_2S abundance remains constant, with a large scatter for $T < 18$ K. Interestingly enough, no trend is observed in the relation between HDS/H_2S abundance ratios and molecular hydrogen density, $n(H_2)$, within our uncertainties. The lack of correlations of HDS/H_2S with molecular hydrogen density is intriguing. As long as the dust temperature is lower than ∼18 K, higher densities induce higher CO depletions, which favour the enhancement of H_3^+ abundances and the abundances of deuterated ions H_2D^+, D_2H^+, D_3^+ in cold gas. Moreover, the deuteration on grain surfaces also depends on the amount of H_2D^+, D_2H^+, D_3^+ in gas phase since the dissociative electronic recombination of these atoms is producing the D atoms that will eventually accrete on the grain surfaces. The large scatter in the observed values could hinder any trend with the density, given the small number of points in our sample. No clear trend is observed in the case of the relation between the HDS/H_2S ratio and the extinction, either.

Differences between clouds are less evident in the case of double deuteration values (D_2S/H_2S abundance ratios). There is only one detection in Taurus, with no significant upper limits in the case of other Taurus objects, which prevents a good comparison with Perseus, and it is a similar situation with Orion. Analogously, we cannot establish the possible existence of a trend in the relation of this ratio with kinetic temperature or extinction.

The D_2S/HDS abundance ratio provides information about the relation between single and double deuteration. We have only five detections for the three clouds, which makes it difficult to find any trend. No clear trend is observed in the case of temperature and visual extinction. A hint of trend is observed in the right panel of Fig. 3, with the D_2S/HDS abundance ratio increasing with density. This is consistent with results obtained by Chacón-Tanarro et al. (2019) analysing the emission of deuterated H_2CO towards the pre-stellar core L1544.

6.2. Comparison with other interstellar sources

The deuterium fraction is sensitive to the physical conditions of the source, such as temperature, CO depletion, H_2 density, and OPR. Moreover, the deuterium fraction in the gas phase is

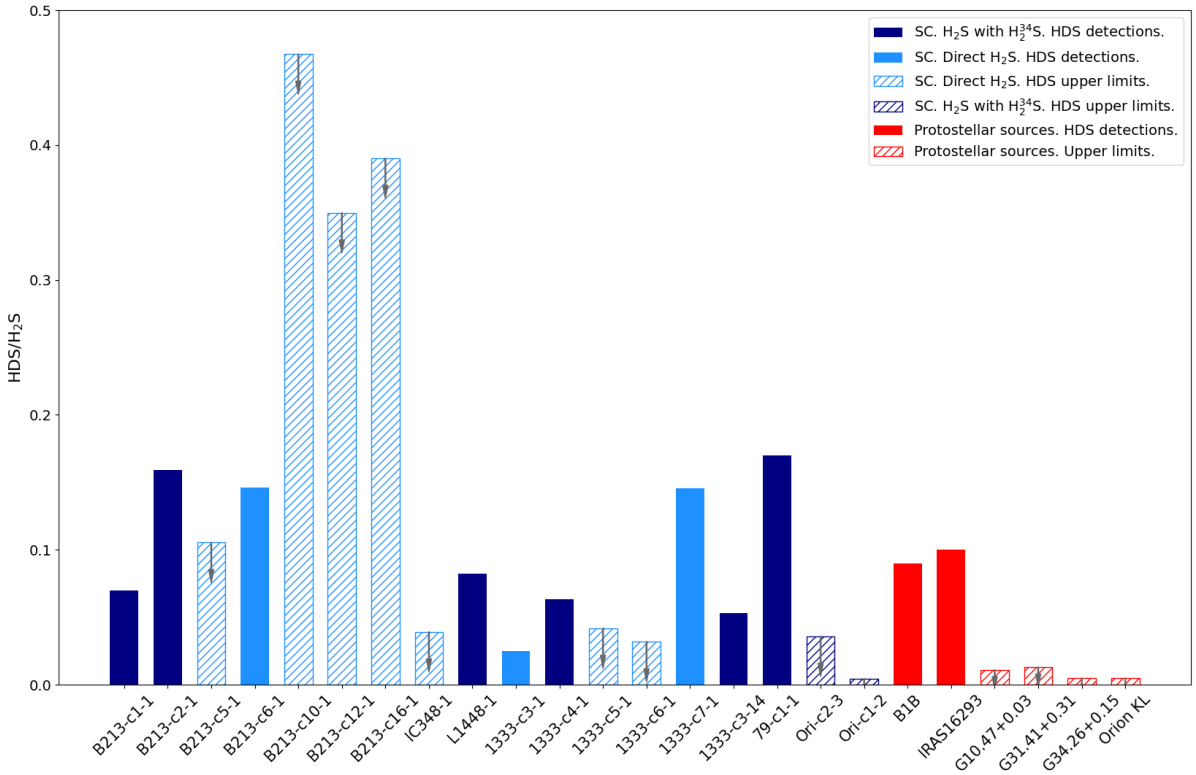

Fig. 4. Comparison of H_2S deuterium fraction, HDS/H_2S, in starless cores (blue) and protostellar sources (red). The bar pattern indicates the direct detection (solid) or determination of upper limits (dashed) of the HDS emission. The starless cores' dataset is colour-coded according to the method applied for the estimation of the H_2S abundance, as shown in the legend. References: Starless cores: This work. B1b: This work. IRAS 16293: van Dishoeck et al. (1995). G10.47+0.03, G31.41+0.31 and G34.26+0.15: Hatchell et al. (1999). Orion KL: Crockett et al. (2014).

thought to vary along the dynamical evolutionary stages of the star formation process, increasing towards the onset of star formation and decreasing afterwards, due to the heating produced by the newly formed stellar object. Comparing deuterated emission from different interstellar sources allows us to determine the effects of physical conditions and stellar formation evolution on deuterium fraction.

Figure 4 shows a comparison between the values of the HDS/H_2S abundance ratio obtained for our starless core sample and other sources from the literature. H_2S deuterated compounds have been observed in only a few other interstellar sources, and in several cases only upper limits are estimated, but those limits are significant in comparison with the values obtained for our sources. Within our sample, it should be noted that no significant difference is found between the HDS/H_2S ratio of B1, already classified as a Class 0 source although extremely young (Gerin et al. 2015, 2017; Fuente et al. 2016, 2017; Marcelino et al. 2018), and the starless cores of the sample. Starless core values are also comparable to the one obtained by van Dishoeck et al. (1995) for the hot corino IRAS 16293, where the high temperature of the central region would be thought to produce a decrease in the fraction of deuterated molecules in the gas phase. This result, if confirmed, would point again towards the possibility of H_2S deuterated compounds mainly formed by surface reactions (see Sect. 6.1). If these compounds are subsequently evaporated due to the increasing temperature produced by the new stellar object, but not utterly processed in the gas phase, deuterium fraction would remain comparable to that of the starless core phase. However, it is also possible that this is the consequence of an observational bias, where observed values of B1b and IRAS 16293 are still produced by their cold envelopes instead in the compact hot corinos. Interferometric observations with high spatial resolution are needed to resolve the central region of this kind of source and confirm or discard this hypothesis. The effect of temperature is indeed observed in the hot, massive star-forming clouds G10.47+0.03, G31.41+0.31, and G34.26+0.15 observed by Hatchell et al. (1999), where only the upper limits are measured but where these are significantly lower than those obtained for the starless cores in our sample. Figure 4 also shows that the HDS/H_2S values of the starless core sample are clearly higher than the upper limit obtained for Orion KL. This upper limit was derived by Crockett et al. (2014), who analysed the H_2S emission towards the Orion KL hot core, estimating a rotational temperature, $T_{\rm rot}$, of 141 K. They therefore analysed the H_2S emission coming from the inner envelope, where high temperature produces the sublimation of the ice grain mantles built up during the pre-stellar core phase. Traditionally, two explanations have been proposed to explain the differences in the deuteration between hot corinos and hot cores associated with massive star-forming regions (Fuente et al. 2005, 2014; Ceccarelli et al. 2014). One possibility is that the hot cores associated with massive stars are older and/or significantly denser than those surrounding low-mass objects. In this case, gas phase chemistry could have had the time to reset the deuterium fractions to values close to the cosmic D/H ratio. An alternative explanation is that the temperature of the envelope material accreting onto the high-mass protostars was higher than in the case of low mass stars, already reducing the deuterium fractionation efficiency before the hot core phase. We have observed lower H_2S deuterium fractions in the starless cores located in Perseus and Orion than in Taurus. This suggests that the low H_2S deuteration in hot cores might indeed be inherited from the pre-stellar phase when

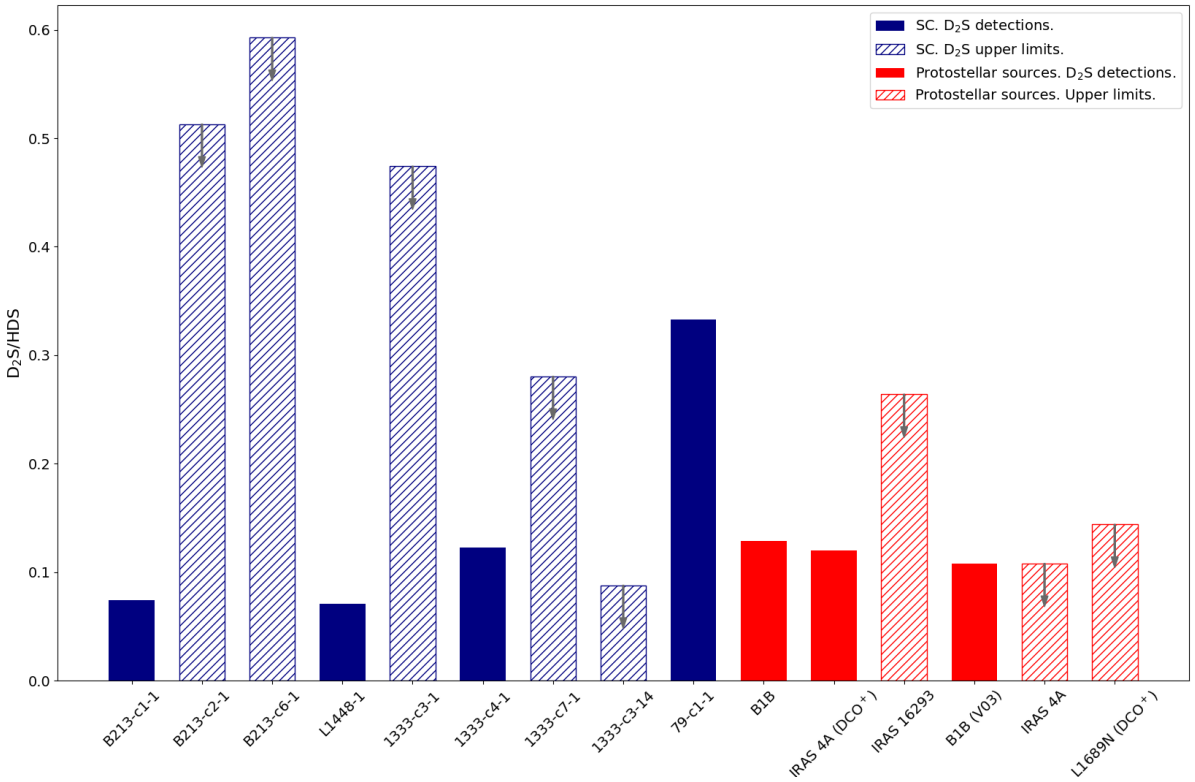

Fig. 5. Comparison of double deuterium fraction, D_2S/HDS, between starless cores (blue) and protostellar sources (red). The bar pattern indicates the direct detection of the ratio lines (solid) or determination of upper limits in the case of D_2S emission (dashed), as indicated in the legend. References: starless cores: This work. B1b: this work and Vastel et al. (2003, marked in the plot as V03). Rest of protostellar sources: Vastel et al. (2003).

the ice mantles are grown. However, our observations towards Orion A are limited to two positions, clearly insufficient to establish firm conclusions. A high sensitive and spatial resolution survey of HDS in a large sample of starless cores in Orion is required in order to get a deeper insight into the H_2 deuteration in Orion.

Analogously, a comparison between the D_2S/HDS abundance ratio values obtained for our sample and other interstellar sources from the literature is shown in Fig. 5. In this case only Vastel et al. (2003) provided observations of double deuterated H_2S for five sources, with two detections and three upper limits. The value obtained in this work for B1b is in good agreement with that obtained by these authors for the same source. Although the number of D_2S detections is limited and therefore establishing a firm conclusion is risky, our data may suggest that the D_2S/HDS abundance ratio is increasing along the starless core evolution, becoming maximum close to the Class 0 phase.

6.3. Comparison with other molecules

The deuterium fraction is a powerful tool with which to study the evolution of material during the star and planetary formation process. As an example, the observation and modelling of water and its deuterated isotopologues has established that a substantial fraction of the water in the Solar System has been inherited from the pre-stellar core, where the Sun was formed (Cleeves et al. 2014; van Dishoeck et al. 2021). Conclusive evidence of this was found in the high abundances of the doubly deuterated water, highlighting how powerful it is to use deuteration as a probe of inheritance. Moreover, molecules with multiple deuteration provide crucial constraints not only to the deuteration processes involved, but also to the formation of the main species.

In order to be able to compare between D/H ratios observed for different molecules, it has to be taken into account that the deuterium fraction of a molecule does not directly correspond to the abundance ratio between the deuterated and the main isotopologues, as presented in Appendix B of Manigand et al. (2019) and Appendix C of Drozdovskaya et al. (2022). When the chemical group containing D isotopes has at least two bonds to H or D atoms, it is not possible to distinguish between the different arrangements of H and D. The probability of a D atom replacing a H atom at a specific location in a certain functional group (-XH_n) is a statistically independent event. The number of indistinguishable combinations with i deuterium atoms at n potential sites in a specific functional group is the statistical correction that has to be applied to the abundance ratio of two isotopologs to obtain the molecular deuteration fraction, in other words the D/H ratio, of a molecule. The relation between the abundance ratio and the D/H ratio is

$$\frac{XH_{n-i}D_i}{XH_n} = \binom{n}{i}\left(\frac{D}{H}\right)^i_{XH_n}, \quad (1)$$

as presented in Manigand et al. (2019), where n is the number of valence of the X group, i is the number of D attached to the X group, and $\binom{n}{i} = \frac{n!}{i!(n-i)!}$ is the number of arrangements of i into n. When the D/H ratio of an isotopologue is considered relative to another isotopologue that already contains j deuterium atoms in that functional group, instead of the isotopologue without

Table 4. Relations between the abundance ratio and the D/H ratio.

Abundance ratio		D/H ratio prescription
HDS/H_2S	=	2 (D/H)
D_2S/HDS	=	1/2 $(D/H)_{HDS}$
$HDCS/H_2CS$	=	2 (D/H)
$D_2CS/HDCS$	=	1/2 $(D/H)_{HDCS}$
HDO/H_2O	=	2 (D/H)
D_2O/HDO	=	1/2 $(D/H)_{HDO}$
$HDCO/H_2CO$	=	2 (D/H)
$D_2CO/HDCO$	=	1/2 $(D/H)_{HDCO}$
CH_2DOH/CH_3OH	=	3 (D/H)
CH_3OD/CH_3OH	=	(D/H)
CHD_2OH/CH_2DOH	=	$(D/H)_{CHD_2OH}$
cC_3HD/cC_3H_2	=	2 (D/H)
cC_3D_2/cC_3HD	=	1/2 $(D/H)_{cC_3HD}$

deuterium, then this leads to the relation

$$\frac{XH_{n-i}D_i}{XH_{n-j}D_j} = \frac{\binom{n}{i}}{\binom{n}{j}} \left(\frac{D}{H}\right)^{i-j}_{XH_{n-j}D_j}, i > j \geq 0. \quad (2)$$

The different relations between abundance ratio and D/H ratio for the isotopologues considered in this paper are provided in Table 4.

Figure 6 shows the D/H ratios, including the respective statistical corrections, of simply deuterated isotopologues of H_2S, H_2CS, H_2CO, c-C_3H_2, and CH_3OH measured in our starless core sample, as well as other starless cores and young star-forming sources published in the literature. First of all, this allows a direct comparison between the D/H values measured for H_2S in this work with the D/H ratio derived from the HDCS abundances reported by Esplugues et al. (2022) in the same sample. This comparison reveals that the D/H is systematically lower in H_2S than in H_2CS in starless cores. One could think that this difference is related to the different formation routes for these two molecules. While thioformaldehyde (H_2CS) can be formed through gas-phase reactions and on grain surfaces (Esplugues et al. 2022), the formation of H_2S, and probably its deuteration, should occur only on the grain surfaces (Oba et al. 2019). Alternatively, lower deuteration of H_2S might also be related to an earlier formation time of this molecule in the collapsing process of the starless core, with higher temperatures and worse conditions for deuteration. It is also interesting to compare the deuterium fractions of H_2S with that of methanol (CH_3OH). Ambrose et al. (2021) observed the single-deuterated methanol compound CH_2DOH in a sample of starless cores in the B10 region of Taurus. They observed D/H methanol ratios in the same range of values as those that we have obtained for H_2S in our sample. Methanol is formed in the cold interior of molecular clouds by successive hydrogenation of CO on the icy grain mantles (Vasyunin et al. 2017; Punanova et al. 2022) while H_2S is more abundant on the cloud surface (Navarro-Almaida et al. 2020). One would expect higher values of deuterium fraction in CH_2DOH than in H_2S. On the contrary, the two molecules present similar values. Interestingly, CH_2DOH with CH_3OD present different D/H values, CH_3OD being less abundant than CH_2DOH. To complete this comparison, we include the D/H ratio of c-C_3H_2 obtained by Chantzos et al. (2018) and Giers et al. (2022) in a sample of starless cores and protostars. This molecule is thought to be formed mainly in gas phase. Its D/H ratio is similar to those of CH_3OH and H_2S, and lower than H_2CS.

When considering young protostellar objects, classified as Class 0, it is important to differentiate between single-dish and interferometric measurements. Single-dish measurements do not allow to discern the origin of the emission within the protostellar envelope, except in the case of multi-transitional studies, which are less common. In Fig. 6 we differentiate between those values obtained with single-dish observations and those related to interferometric observations using different symbols. Restricting ourselves to single-dish measurements, we observe a wider dispersion of the data, but the D/H values are in the same range as those observed in the case of starless cores. There is a scarcity of HDS detections in this kind of source but, as seen in Fig. 4, they are in good agreement with values obtained in our work for starless cores. Moreover, in these sources there are a certain number of detections of formaldehyde (H_2CO), which share the same range of values as that obtained for HDCS, supporting the idea that they may be formed in similar conditions. In the case of methanol, most of the deuterium fraction values obtained, both for CH_2DOH and CH_3OD, are lower than those of HDS, HDCS, and HDCO, with the exception of four CH_2DOH detections obtained by Parise et al. (2006) for IRAS16293, IRAS2, IRAS4A, and IRAS4B. Some of these sources also have detections of singly deuterated water, HDO, the deuterium fraction of which is smaller than that of any of the other considered molecules. While single-dish detections of Class 0 sources share the same range of deuterium fraction values as those obtained for starless cores, interferometric values show a clear decreasing trend with respect to these earlier stage sources. This difference points again to the idea that single-dish observations may be detecting only the emission of the cold envelope, while interferometric observations manage to detect the effect of the increasing temperature of the protostar in the innermost layers of the gas.

We also compare our results in Fig. 6 with values obtained for one Class I source, SVS13A, with detections of deuterated formaldehyde and methanol (Bianchi et al. 2017a), and of thioformaldehyde (Bianchi et al. 2019). HDCO and HDCS deuterium fractions are in the same range of values as those of Class 0 sources. On the contrary, CH_2DOH shows a clear decrease with respect to values of younger sources, an effect which cannot be associated with observational techniques since these detections were made with the IRAM 30 m telescope.

Finally, we observe a general trend (in all molecules) of decreasing deuterium fraction values when considering detections of these deuterated molecules in massive star-forming regions, an effect that is also in this case even more pronounced in the case of interferometric observations. Again, we consider that we are observing the effect of higher temperatures, creating less favourable environments for deuteration processes.

The study of double deuteration also provides information about the formation and deuteration processes of molecules. In particular, in the case of species forming on the grain surfaces, then the relation $D_2/D = 0.25$ D/H would hold as long as the distribution of D atoms were purely statistical, meaning just proportional to the D/H ratio, (Ceccarelli et al. 2014). Figure 7 represents the double deuteration fraction, that is the abundance ratio of the double deuterated compound to the simple deuterated compound with the corresponding statistical correction, as a function of the simple D/H ratio of the corresponding surface molecule. The statistical relation $D_2/D = 0.25$ D/H (red line in Fig. 7) is not fulfilled for any of the considered molecules, a similar result to the one obtained by Ceccarelli et al. (2014). They provide the plausible explanation that this is the

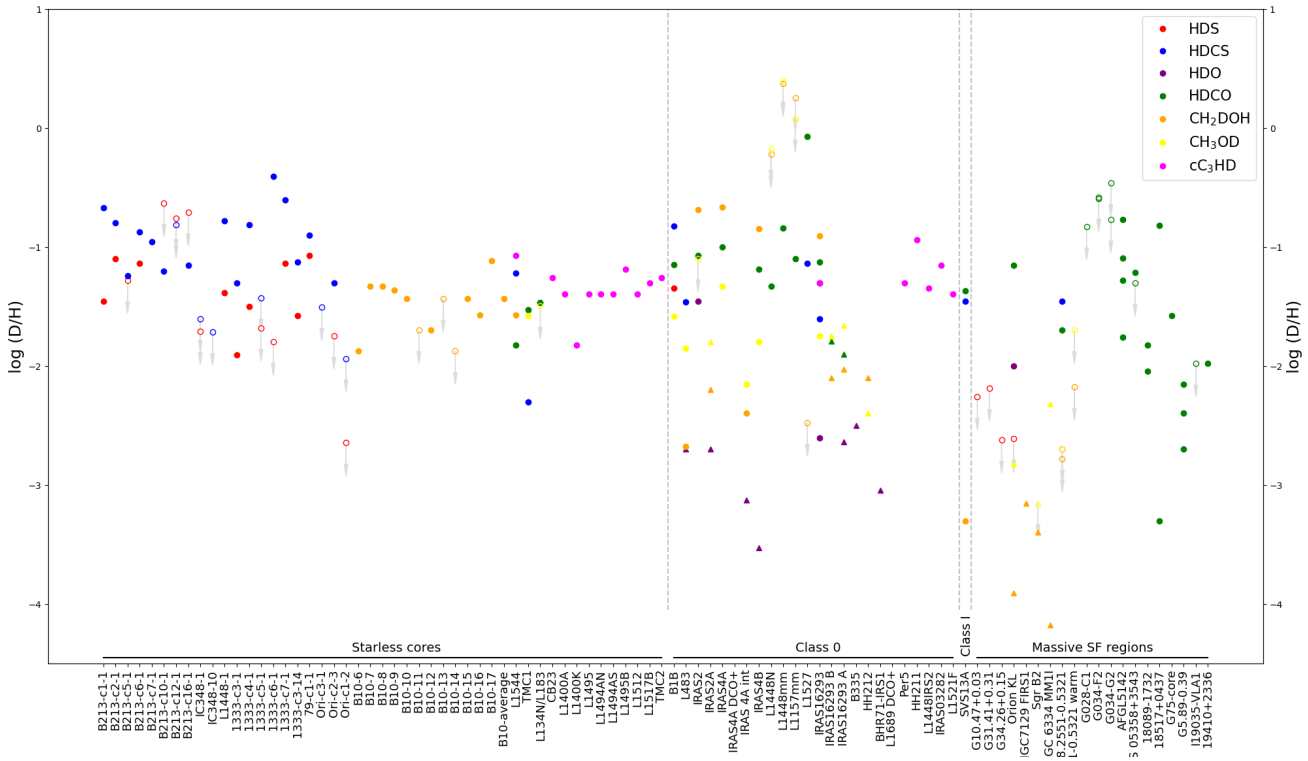

Fig. 6. Comparison between D/H ratios of simply deuterated molecules, including the respective statistical corrections (see text), for several early-stage star-forming sources. Data are colour-coded corresponding to the different molecules shown in the legend. Filled symbols represent direct detections of the corresponding deuterated molecule. Open symbols represent the upper limits. Circles represent data obtained with single-dish observations. Triangles represent data obtained with interferometric observations. Dashed grey lines are a guide to distinguishing different star-forming stages. Notes: References per source: Starless cores GEMS sample: This work and Esplugues et al. (2022). B10-6 to B10-17 starless cores in Taurus: Ambrose et al. (2021). L1544: Chacón-Tanarro et al. (2019), Spezzano et al. (2022b), and Giers et al. (2022). TMC1: Minowa et al. (1997) and Turner (2001). L134N/L183: Turner (2001). CB23, L1400A, L1400K, L1495, L1495AN, L1495AS, L1495B, L1512, L1517B, and TMC2: Chantzos et al. (2018). B1b: This work, Marcelino et al. (2005), and Turner (2001). L483: Agúndez et al. (2019) and Jensen et al. (2021). IRAS2/IRAS2A: Coutens et al. (2014), Liu et al. (2011), Parise et al. (2006), and Taquet et al. (2013a). IRAS4A/IRAS4A DCO$^+$/IRAS4A interferometry: Parise et al. (2006), Taquet et al. (2013a), Taquet et al. (2019), and Vastel et al. (2003). IRAS4B: Parise et al. (2006) and Persson et al. (2014). L1448N/L1448mm: Parise et al. (2006). L1157mm: Parise et al. (2006). L1527: Parise et al. (2006), Sakai et al. (2009), and Yoshida et al. (2019). IRAS16293: Butner et al. (2007), Coutens et al. (2012), Drozdovskaya et al. (2018), Parise et al. (2006), van Dishoeck et al. (1995), Vastel et al. (2003), and Chantzos et al. (2018). IRAS16293A: Drozdovskaya et al. (2022), Manigand et al. (2020), and Persson et al. (2013). IRAS16293 B: Drozdovskaya et al. (2022), Jørgensen et al. (2018), and Persson et al. (2018). B335: Jensen et al. (2021). HH212: Bianchi et al. (2017b) and Taquet et al. (2019). BHR71-IRS1: Jensen et al. (2019). L1689 DCO$^+$: Vastel et al. (2003). Per5, HH211, L1448IRS2, IRAS03282, and L1521F: Chantzos et al. (2018). SVS13A: Bianchi et al. (2017a, 2019). G10.47+0.03, G31.41+0.31, and G34.26+0.15: Hatchell et al. (1999). Orion KL: Bergin et al. (2002), Crockett et al. (2014), Lis et al. (2002), Taquet et al. (2019), and Turner (1990). NGC7129 FIRS2: Fuente et al. (2014). Sgr B2: Belloche et al. (2016). NGC 6334 MM1I: Bøgelund et al. (2018). G328.2551-0.5321/G328.2551-0.5321 warm: Bouscasse et al. (2022). AFGL5142, IRAS 05358+3543, and G5.89-0.39: Zahorecz et al. (2017, 2021). G028-C1, G034-F2, G034-G2, 18089-1732, 18517+0437, G75-core, I19035-VLA1, and 19410+2336: Zahorecz et al. (2021).

consequence of the D and D_2-bearing compounds being formed at different times on the grain surfaces, related to different D/H ratios in the gas. Within this scenario the single-dish detections of methanol, closer to the statistical value, may be related to formation in a short time interval, while the formation of other molecules may occur in larger intervals of times, where the single and double deuterated forms may not have inherited the same D/H atomic ratio. As discussed in next section, new experimental results suggest that these differences could also be related to H-D substitution reactions on the grain surfaces (Oba et al. 2019).

7. Discussion

Single and multiple deuterium fractions provide essential information about the formation and evolution of important molecules in the interstellar medium. This is the case, for example, for molecules formed with an interplay of gas-phase and grain-surface chemistry, such as formaldehyde (Zahorecz et al. 2021) and thioformaldehyde. H_2CS is formed both in the gas phase (mainly from atomic S, Esplugues et al. 2022) and on the surface of dust grains, by the addition of H atoms to CS (Spezzano et al. 2022b). Another molecule of interest regarding the grain surface deuteration processes is methanol. In pre-stellar cores, once CO freezes out onto the surfaces of dust grains, it can either be stored in the icy mantles or react with other elements, particularly atomic hydrogen. In the latter case, CO is first transformed into HCO, then formaldehyde and eventually into methanol. Another example is water, where, as already mentioned in Sect. 6.3, the observation and modelling of the main compound and its deuterated isotopologues established that a substantial fraction of the water in the Solar System has been

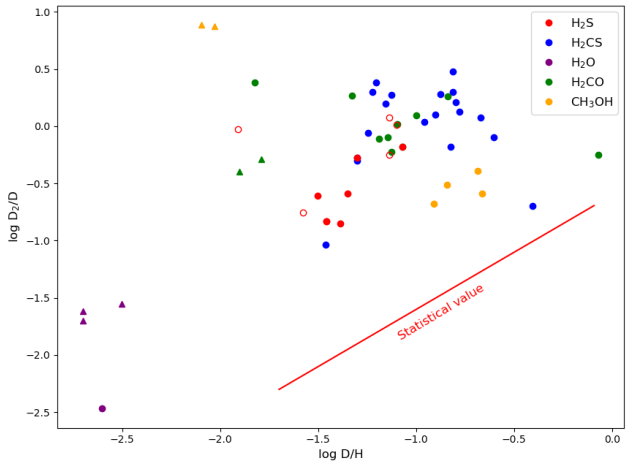

Fig. 7. D/H ratio of double deuterated molecules as a function of the D/H ratio of the corresponding simple deuterated molecules, including statistical corrections in both cases (see text). Only starless cores and Class 0 sources are included, for direct comparison. The dataset is colour-coded according to the corresponding molecule, as indicated in the legend. In the case of methanol, the single deuterated molecule is CH_2DOH. For both ratios, circles represent data obtained with single-dish observations for both ratios, while triangles represent data obtained with interferometric observations. In the case of H_2S, open symbols are the upper limits, corresponding to the sources of this work, where only HDS was directly detected. The red line shows the statistical value if the D atoms were statistically distributed in the molecules formed in the grain surfaces (see text).

inherited from the pre-stellar core, where the Sun was formed (Cleeves et al. 2014; van Dishoeck et al. 2021).

In Fig. 6, we compare the deuteration (D/H) ratio of H_2S with those obtained for H_2CS, H_2CO, c-C_3H_2, H_2O, and CH_3OH in different star-forming regions. As expected, there is a trend for the deuterium fraction to be at its maximum in starless cores and the cold envelope of Class 0 objects, and to decrease in more evolved Class I targets and massive star-forming regions. This is a general behaviour shared by all the considered species; nevertheless, there are significant differences between species when carrying out a more detailed analysis. In particular, for starless cores, the highest values of D/H are found for HDCS and HDCO, while HDS presents lower values similar to those found for deuterated CH_3OH and c-C_3H_2.

For Class 0 objects, single-dish results (dotted points in Fig. 6) of D/H for H_2CO, H_2CS, H_2S, and CH_3OH are in the same range as for starless cores. However, if we consider interferometric results (triangles in Fig. 6), we observe a significant decrease in the D/H results with respect to the single-dish observations due to the fact that, in the former case, we are observing only the hot corino. Regardless of the observational technique, single-dish or interferometry, the lowest values of D/H in Class 0 objects are found for H_2O, being significantly lower than those for methanol and the other species.

In Fig. 7, we compare the results of the double to single deuterated ratios of CH_3OH, H_2O, and H_2S. In the case of those species that form on the grain surfaces, the relation D_2/D = 0.25 D/H would hold as long as the distribution of D atoms were purely statistical, meaning just proportional to the D/H ratio at formation (Ceccarelli et al. 2014). Our first result is that the D_2/D ratio is higher than the statistical value for all of them. Moreover, the deuteration is very different from one compound to another, CH_3OH being the one with higher deuteration levels, followed by H_2S, and H_2O, which is the one with the lowest deuteration values. The difference between the deuteration of H_2O and CH_3OH has been interpreted by different authors in terms of an evolutionary sequence (see, e.g., the review by Ceccarelli et al. 2014): the O hydrogenation leading to water occurs first and, once formed, water remains frozen on the grains (Hollenbach et al. 2009). The formation of H_2CO by CO hydrogenation, and subsequently the formation of CH_3OH, occurs later (Cazaux et al. 2011; Taquet et al. 2012). Since the deuteration of molecules on the grain surface is governed by the gas D/H ratio at formation, which increases with decreasing temperature along the evolution of the pre-stellar core, larger deuterium fractions correspond to larger D/H gas ratios, and therefore to a later formation and deuteration of the molecules.

This explanation may work for CH_3OH and H_2O, but it would not explain the difference between H_2O and H_2S, since both are expected to form in the first stages of the cloud collapse. In order to understand the difference between these two species, we need to take into account the occurrence of H-D and D-H substitution reactions on the grain surfaces (Oba et al. 2012, 2019). H_2O is only deuterated during its formation process (Oba et al. 2012; Taquet et al. 2013b), while H_2S can also be deuterated through H–D substitution processes on the grain surfaces after their formation (Oba et al. 2019). The reverse reaction, D-H substitution, can also occur, thus it could be thought that this mechanism may in principle diminish or suppress the deuteration level of H_2S. However, laboratory experiments carried out by Oba et al. (2019) show that chemical desorption is an effective desorption mechanism of H_2S and its deuterated compounds. Once HDS is formed from H_2S via H–D substitution, it could be released to the gas phase via chemical desorption, while on the contrary the desorbed HDS undergoes D-H substitution only when readsorbed onto the grain surfaces. Therefore, this mechanism may increase the deuteration levels of H_2S in the gas phase, potentially exceeding the atomic D/H ratio in the environment at formation. The efficiency of this mechanism in the ISM conditions should be further explored.

Surface H-D substitution reactions may also occur in the case of methanol to form CH_2DOH and CHD_2OH. In this case, the extremely low occurrence of D–H substitution reactions (Nagaoka et al. 2007) could help to maintain high levels of deuteration in these species in the gas phase. In other words, once CH_2DOH and CHD_2OH are formed through the H–D substitution reactions of CH_3OH, it could be difficult to return to non-deuterated methanol. In order to confirm this interpretation, it is interesting to compare the deuteration in oxygen (CH_3OD) with that in carbon (CH_2DOH and CHD_2OH). Since abstraction of the H from OH is not possible, the CH_3OD/CH_3OH should be significantly lower than the CH_2DOH/CH_3OH ratio and closer to the HDO/H_2O ratio. This is indeed in agreement with observational data, which shows that (D/H) for CH_3OD is significantly lower, by more than one order of magnitude, than for CH_2DOH (see Fig. 6). This supports the interpretation that the differences in the deuteration of H_2O, H_2S, and CH_3OH are not only due to differences in the D/H ratio at their formation but also to the subsequent H–D and D-H substitution reactions.

Deuteration is a complex process that depends on the initial physical conditions and H_2 OPR, as well as on the evolution of the molecular cloud during its collapse to form protostars. To explain, at least qualitatively, the observed D_2/D and D/H values in H_2O, H_2S, and CH_3OH, the H-D and D-H substitution reactions on the grain surface and chemical desorption need to be considered. A detailed chemical model including all these

effects is necessary to get a deeper insight into the evolution of deuteration during the star formation process.

8. Summary and conclusions

This work is aimed at investigating the deuteration of H_2S in cold cores. Although HDS was first detected by van Dishoeck et al. (1995) towards the cold star-forming core IRAS 16293 almost two decades ago, the deuterium fraction of H_2S in starless cores had not been studied thus far. We used observations of the GEMS IRAM 30 m Large Program, as well as complementary observations with the 30m IRAM telescope. We searched for HDS and D_2S in 19 starless cores selected from the whole GEMS sample, located in the Taurus, Perseus, and Orion molecular clouds, characterised by different star formation activities. HDS emission has been detected in ten of these starless cores and D_2S emission has been detected in five, which significantly increases the number of detections of these compounds in star-forming regions. Upper limits have been derived for the rest of the sample. The HDS and o-D_2S column densities were derived using the RADEX code and the recent HDS and o-D_2S collisional coefficients published by Dagdigian (2022), providing the most accurate values of these compound abundances.

We analysed the H_2S single and double deuterium fraction with regard to their relation with the corresponding cloud's physical parameters, comparisons with values obtained for other interstellar sources, and comparisons with observed deuterium fractions observed of other molecules that may be related to H_2S in terms of formation paths or the influence of sulphur abundance. Our results can be summarised as follows:

– Regarding the relation between H_2S deuteration and the cloud's physical conditions, we find that the value of the HDS/H_2S abundance ratio shows a decreasing trend with increasing cloud kinetic temperature, displaying values of 0.1−0.3 in starless cores with $T < 18$ K. This relation is expected, since low temperatures favour higher deuteration values. We have not detected HDS in warmer cores, which show the upper limits of X(HDS)/X(H_2S) < 0.03. No trend of X(HDS)/X(H_2S) is found with molecular hydrogen density and/or visual extinction. The five starless cores with D_2S detections show values of X(D_2S)/X(HDS) ∼ 0.05−0.3. The low number of detections prevents us from carrying out a reliable study of the dependence of this ratio on the cloud's physical conditions.
– The comparison of the HDS/H_2S in this work sample with other interstellar sources from the literature reveals a similar range of values with respect to Class 0 sources. This may be the consequence of an observational bias where observed values for Class 0 sources using single-dish telescopes are still produced by their cold envelopes. Interferometric observations are needed to clarify this issue. A comparison of the D_2S/HDS abundance ratio with other interstellar sources suggests that this ratio is increasing along the starless core evolution, but the limited number of detections and sources prevents a firm conclusion.
– We compared the H_2S deuterium fraction with that of H_2O, H_2CS, H_2CO, c-C_3H_2, and CH_3OH in other interstellar sources. As a general trend, the deuteration of all these compounds decreases with temperature during the star formation process, with lower values in Class I sources and massive star-forming regions. Focusing on starless cores and young Class 0 objects, H_2CS and H_2CO present higher deuterium fractions that H_2O, H_2S, c-C_3H_2, and CH_3OH. We interpret this difference as the consequence of different formation and deuteration processes: H_2CS and H_2CO are mainly formed and deuterated through gas-phase reactions and on grain surfaces.The cyclic hydrocarbon c-C_3H_2 is thought to be formed in the gas phase while H_2O, H_2S, and CH_3OH are thought to form on the grain surfaces. Interestingly enough, single and double deuterations of water are one order of magnitude lower than those of H_2S, even though both H_2O and H_2S are formed by hydrogenation of the O and S atoms, respectively. Higher deuterium fractions are observed in the case of CH_3OH.
– We propose that the observed behaviours of the D_2/D and D/H values in H_2O, H_2S, and CH_3OH are the consequence of a complex surface chemistry involving H-D and D-H substitution, different chemical desorption efficiencies, and the chemical evolution of starless cores. While H_2O is only deuterated during its formation process, H_2S can be deuterated, afterwards, through H–D substitution processes on the grain surfaces. The reverse reaction, D-H substitution, can also occur on the grain surfaces. However, after its formation, HDS can be released into the gas phase via chemical desorption, thus keeping high deuteration levels of H_2S in the gas Oba et al. (2019). The processes are similar for deuterated methanol (on carbon) but the relative importance is different from H_2S. In the case of methanol, once deuterated methanol such as CH_2DOH and CHD_2OH is formed through the H–D substitution reactions of CH_3OH, and the inverse reactions have lower rates than in the case of H_2S Nagaoka et al. (2007). Abstraction of the H from OH is not possible, and for this reason the CH_3OD/CH_3OH is significantly lower than the CH_2DOH/CH_3OH ratio.

This work confirms once again that the deuterium fraction provides essential information about the formation and evolution of interstellar molecules. Further specific interferometric observations are needed to keep clarifying the evolution of deuteration during the star formation processes, while a full understanding of deuteration processes requires laboratory experiments that clarify the complex ice chemistry.

Acknowledgements. We thank the Spanish Ministerio de Ciencia e Innovación for funding support through project PID2019-106235GB-I00. A.F. is grateful to the European Research Council (ERC) for funding under the Advanced Grant project SUL4LIFE, grant agreement No 101096293. D.N.A. acknowledges funding support from Fundación Ramón Areces through its international postdoc grant program. R.M.D. has received funding from "la Caixa" Foundation, under agreement LCF/BQ/PI22/11910030. I.J.-S. has received support from grant No. PID2019-105552RB-C41 by the Spanish Ministry of Science and Innovation/State Agency of Research MCIN/AEI/10.13039/501100011033. We thank the anonymous referee for valuable comments that improved the manuscript.

References

Agúndez, M., & Wakelam, V. 2013, Chem. Rev., 113, 8710
Agúndez, M., Marcelino, N., Cernicharo, J., Roueff, E., & Tafalla, M. 2019, A&A, 625, A147
Albertsson, T., Semenov, D. A., Vasyunin, A. I., Henning, T., & Herbst, E. 2013, ApJS, 207, 27
Ambrose, H. E., Shirley, Y. L., & Scibelli, S. 2021, MNRAS, 501, 347
André, P., Men'shchikov, A., Bontemps, S., et al. 2010, A&A, 518, L102
Anglada, G., Estalella, R., Pastor, J., Rodriguez, L. F., & Haschick, A. D. 1996, ApJ, 463, 205
Bacmann, A., Lefloch, B., Ceccarelli, C., et al. 2003, ApJ, 585, L55
Bacmann, A., Faure, A., Hily-Blant, P., et al. 2020, MNRAS, 499, 1795
Bally, J., Langer, W. D., Stark, A. A., & Wilson, R. W. 1987, ApJ, 312, L45
Belloche, A., Müller, H. S. P., Garrod, R. T., & Menten, K. M. 2016, A&A, 587, A91
Benson, P. J., & Myers, P. C. 1989, ApJS, 71, 89
Bergin, E. A., Alves, J., Huard, T., & Lada, C. J. 2002, ApJ, 570, L101

Bernard, J.-P., Paradis, D., Marshall, D. J., et al. 2010, A&A, 518, L88
Bianchi, E., Codella, C., Ceccarelli, C., et al. 2017a, MNRAS, 467, 3011
Bianchi, E., Codella, C., Ceccarelli, C., et al. 2017b, A&A, 606, L7
Bianchi, E., Ceccarelli, C., Codella, C., et al. 2019, ACS Earth Space Chem., 3, 2659
Bøgelund, E. G., McGuire, B. A., Ligterink, N. F. W., et al. 2018, A&A, 615, A88
Bohlin, R. C., Savage, B. D., & Drake, J. F. 1978, ApJ, 224, 132
Bouscasse, L., Csengeri, T., Belloche, A., et al. 2022, A&A, 662, A32
Brown, P. D., & Millar, T. J. 1989, MNRAS, 240, 25P
Butner, H. M., Charnley, S. B., Ceccarelli, C., et al. 2007, ApJ, 659, L137
Cambrésy, L. 1999, A&A, 345, 965
Caselli, P., & Ceccarelli, C. 2012, A&ARv, 20, 56
Caselli, P., Walmsley, C. M., Zucconi, A., et al. 2002, ApJ, 565, 344
Cazaux, S., Caselli, P., & Spaans, M. 2011, ApJ, 741, L34
Ceccarelli, C., Vastel, C., Tielens, A. G. G. M., et al. 2002, A&A, 381, L17
Ceccarelli, C., Caselli, P., Bockelée-Morvan, D., et al. 2014, in Protostars and Planets VI, eds. H. Beuther, R. S. Klessen, C. P. Dullemond, & T. Henning (Tucson: University of Arizona Press), 859
Cernicharo, J., & Guelin, M. 1987, A&A, 176, 299
Chacón-Tanarro, A., Caselli, P., Bizzocchi, L., et al. 2019, A&A, 622, A141
Chantzos, J., Spezzano, S., Caselli, P., et al. 2018, ApJ, 863, 126
Cleeves, L. I., Bergin, E. A., Alexander, C. M. O. D., et al. 2014, Science, 345, 1590
Coutens, A., Vastel, C., Caux, E., et al. 2012, A&A, 539, A132
Coutens, A., Jørgensen, J. K., Persson, M. V., et al. 2014, ApJ, 792, L5
Crapsi, A., Caselli, P., Walmsley, M. C., & Tafalla, M. 2007, A&A, 470, 221
Crockett, N. R., Bergin, E. A., Neill, J. L., et al. 2014, ApJ, 781, 114
Dagdigian, P. J. 2020, MNRAS, 494, 5239
Dagdigian, P. J. 2022, MNRAS, 511, 3440
Dalgarno, A., & Lepp, S. 1984, ApJ, 287, L47
Denis-Alpizar, O., Stoecklin, T., Guilloteau, S., & Dutrey, A. 2018, MNRAS, 478, 1811
Dislaire, V., Hily-Blant, P., Faure, A., et al. 2012, A&A, 537, A20
Drozdovskaya, M. N., van Dishoeck, E. F., Jørgensen, J. K., et al. 2018, MNRAS, 476, 4949
Drozdovskaya, M. N., Coudert, L. H., Margulès, L., et al. 2022, A&A, 659, A69
Emprechtinger, M., Caselli, P., Volgenau, N. H., Stutzki, J., & Wiedner, M. C. 2009, A&A, 493, 89
Esplugues, G. B., Viti, S., Goicoechea, J. R., & Cernicharo, J. 2014, A&A, 567, A95
Esplugues, G., Fuente, A., Navarro-Almaida, D., et al. 2022, A&A, 662, A52
Foreman-Mackey, D., Hogg, D. W., Lang, D., & Goodman, J. 2013, ASP, 125, 925
Frau, P., Girart, J. M., & Beltrán, M. T. 2012, A&A, 537, L9
Fuente, A., García-Burillo, S., Gerin, M., et al. 2005, ApJ, 619, L155
Fuente, A., Cernicharo, J., Caselli, P., et al. 2014, A&A, 568, A65
Fuente, A., Cernicharo, J., Roueff, E., et al. 2016, A&A, 593, A94
Fuente, A., Goicoechea, J. R., Pety, J., et al. 2017, ApJ, 851, L49
Fuente, A., Navarro, D. G., Caselli, P., et al. 2019, A&A, 624, A105
Garrod, R. T., Wakelam, V., & Herbst, E. 2007, A&A, 467, 1103
Gatley, I., Becklin, E. E., Mattews, K., et al. 1974, ApJ, 191, L121
Gerin, M., Pety, J., Fuente, A., et al. 2015, A&A, 577, L2
Gerin, M., Pety, J., Commerçon, B., et al. 2017, A&A, 606, A35
Giers, K., Spezzano, S., Alves, F., et al. 2022, A&A, 664, A119
Goldsmith, P. F., Heyer, M., Narayanan, G., et al. 2008, ApJ, 680, 428
Goodman, J., & Weare, J. 2010, Commun. Appl. Math. Comput. Sci., 5, 65
Graedel, T. E., Langer, W. D., & Frerking, M. A. 1982, ApJS, 48, 321
Gratier, P., Majumdar, L., Ohishi, M., et al. 2016, ApJS, 225, 25
Hacar, A., Tafalla, M., Kauffmann, J., & Kovács, A. 2013, A&A, 554, A55
Hama, T., Kouchi, A., & Watanabe, N. 2018, ApJ, 857, L13
Hatchell, J., Thompson, M. A., Millar, T. J., & MacDonald, G. H. 1998, A&A, 338, 713
Hatchell, J., Roberts, H., & Millar, T. J. 1999, A&A, 346, 227
Hatchell, J., Richer, J. S., Fuller, G. A., et al. 2005, A&A, 440, 151
Hatchell, J., Fuller, G. A., & Richer, J. S. 2007a, A&A, 472, 187
Hatchell, J., Fuller, G. A., Richer, J. S., Harries, T. J., & Ladd, E. F. 2007b, A&A, 468, 1009
Hollenbach, D., Kaufman, M. J., Bergin, E. A., & Melnick, G. J. 2009, ApJ, 690, 1497
Imai, M., Sakai, N., López-Sepulcre, A., et al. 2018, ApJ, 869, 51
Jensen, S. S., Jørgensen, J. K., Kristensen, L. E., et al. 2019, A&A, 631, A25
Jensen, S. S., Jørgensen, J. K., Kristensen, L. E., et al. 2021, A&A, 650, A172
Jiménez-Escobar, A., & Muñoz Caro, G. M. 2011, A&A, 536, A91
Johnstone, D., & Bally, J. 1999, ApJ, 510, L49
Johnstone, D., & Bally, J. 2006, ApJ, 653, 383
Jørgensen, J. K., Müller, H. S. P., Calcutt, H., et al. 2018, A&A, 620, A170
Kim, S., Lee, C. W., Gopinathan, M., et al. 2020, ApJ, 891, 169
Knee, L. B. G., & Sandell, G. 2000, A&A, 361, 671
Kutner, M. L., Evans, N. J., I., & Tucker, K. D. 1976, ApJ, 209, 452
Lada, C. J., Alves, J., & Lada, E. A. 1996, AJ, 111, 1964
Ladd, E. F., Lada, E. A., & Myers, P. C. 1993, ApJ, 410, 168
Linke, R. A., & Goldsmith, P. F. 1980, ApJ, 235, 437
Linsky, J. L. 2003, Space Sci. Rev., 106, 49
Lis, D. C., Roueff, E., Gerin, M., et al. 2002, ApJ, 571, L55
Liszt, H. S., Wilson, R. W., Penzias, A. A., et al. 1974, ApJ, 190, 557
Liu, F. C., Parise, B., Kristensen, L., et al. 2011, A&A, 527, A19
Loinard, L., Castets, A., Ceccarelli, C., Caux, E., & Tielens, A. G. G. M. 2001, ApJ, 552, L163
Lombardi, M., Bouy, H., Alves, J., & Lada, C. J. 2014, A&A, 568, C1
Luhman, K. L., Stauffer, J. R., Muench, A. A., et al. 2003, ApJ, 593, 1093
Malinen, J., Juvela, M., Rawlings, M. G., et al. 2012, A&A, 544, A50
Manigand, S., Calcutt, H., Jørgensen, J. K., et al. 2019, A&A, 623, A69
Manigand, S., Jørgensen, J. K., Calcutt, H., et al. 2020, A&A, 635, A48
Marcelino, N., Cernicharo, J., Roueff, E., Gerin, M., & Mauersberger, R. 2005, ApJ, 620, 308
Marcelino, N., Gerin, M., Cernicharo, J., et al. 2018, A&A, 620, A80
Melosso, M., Bizzocchi, L., Sipilä, O., et al. 2020, A&A, 641, A153
Millar, T. J. 2005, Astron. Geophys., 46, 2.29
Millar, T. J., Bennett, A., & Herbst, E. 1989, ApJ, 340, 906
Minh, Y. C., Irvine, W. M., & Ziurys, L. M. 1989, ApJ, 345, L63
Minowa, H., Satake, M., Hirota, T., et al. 1997, ApJ, 491, L63
Mizuno, A., Onishi, T., Yonekura, Y., et al. 1995, ApJ, 445, L161
Nagaoka, A., Watanabe, N., & Kouchi, A. 2007, J. Phys. Chem. A, 111, 3016
Narayanan, G., Heyer, M. H., Brunt, C., et al. 2008, ApJS, 177, 341
Navarro-Almaida, D., Le Gal, R., Fuente, A., et al. 2020, A&A, 637, A39
Neufeld, D. A., Godard, B., Gerin, M., et al. 2015, A&A, 577, A49
Oba, Y., Watanabe, N., Hama, T., et al. 2012, ApJ, 749, 67
Oba, Y., Tomaru, T., Kouchi, A., & Watanabe, N. 2019, ApJ, 874, 124
Onishi, T., Mizuno, A., Kawamura, A., Ogawa, H., & Fukui, Y. 1996, ApJ, 465, 815
Onishi, T., Mizuno, A., Kawamura, A., Tachihara, K., & Fukui, Y. 2002, ApJ, 575, 950
Padoan, P., Cambrésy, L., & Langer, W. 2002, ApJ, 580, L57
Padovani, M., Hennebelle, P., & Galli, D. 2013, A&A, 560, A114
Palmeirim, P., André, P., Kirk, J., et al. 2013, A&A, 550, A38
Parise, B., Ceccarelli, C., Tielens, A. G. G. M., et al. 2002, A&A, 393, L49
Parise, B., Castets, A., Herbst, E., et al. 2004, A&A, 416, 159
Parise, B., Ceccarelli, C., Tielens, A. G. G. M., et al. 2006, A&A, 453, 949
Parise, B., Leurini, S., Schilke, P., et al. 2009, A&A, 508, 737
Persson, M. V., Jørgensen, J. K., & van Dishoeck, E. F. 2013, A&A, 549, L3
Persson, M. V., Jørgensen, J. K., van Dishoeck, E. F., & Harsono, D. 2014, A&A, 563, A74
Persson, M. V., Jørgensen, J. K., Müller, H. S. P., et al. 2018, A&A, 610, A54
Pety, J., Guzmán, V. V., Orkisz, J. H., et al. 2017, A&A, 599, A98
Pineda, J. L., Goldsmith, P. F., Chapman, N., et al. 2010, ApJ, 721, 686
Plunkett, A. L., Arce, H. G., Corder, S. A., et al. 2013, ApJ, 774, 22
Punanova, A., Caselli, P., Pineda, J. E., et al. 2018, A&A, 617, A27
Punanova, A., Vasyunin, A., Caselli, P., et al. 2022, ApJ, 927, 213
Rivière-Marichalar, P., Fuente, A., Goicoechea, J. R., et al. 2019, A&A, 628, A16
Rivière-Marichalar, P., Fuente, A., Le Gal, R., et al. 2021, A&A, 652, A46
Roberts, H., Herbst, E., & Millar, T. J. 2003, ApJ, 591, L41
Rodríguez-Baras, M., Fuente, A., Riviére-Marichalar, P., et al. 2021, A&A, 648, A120
Roueff, E., Tiné, S., Coudert, L. H., et al. 2000, A&A, 354, L63
Roueff, E., Gerin, M., Lis, D. C., et al. 2013, J. Phys. Chem. A, 117, 9959
Roueff, E., Loison, J. C., & Hickson, K. M. 2015, A&A, 576, A99
Sakai, N., Sakai, T., Hirota, T., & Yamamoto, S. 2009, ApJ, 702, 1025
Sandell, G., & Knee, L. B. G. 2001, ApJ, 546, L49
Schmalzl, M., Kainulainen, J., Quanz, S. P., et al. 2010, ApJ, 725, 1327
Scourfield, M., Viti, S., García-Burillo, S., et al. 2020, MNRAS, 496, 5308
Shirley, Y. L., Evans, Neal J., I., Young, K. E., Knez, C., & Jaffe, D. T. 2003, ApJS, 149, 375
Sipilä, O., & Caselli, P. 2018, A&A, 615, A15
Sipilä, O., Caselli, P., & Harju, J. 2015, A&A, 578, A55
Spezzano, S., Fuente, A., Caselli, P., et al. 2022a, A&A, 657, A10
Spezzano, S., Sipilä, O., Caselli, P., et al. 2022b, A&A, 661, A111
Steenbrugge, K. C., de Bruijne, J. H. J., Hoogerwerf, R., & de Zeeuw, P. T. 2003, A&A, 402, 587
Tafalla, M., Santiago-García, J., Myers, P. C., et al. 2006, A&A, 455, 577
Taquet, V., Ceccarelli, C., & Kahane, C. 2012, A&A, 538, A42

Taquet, V., López-Sepulcre, A., Ceccarelli, C., et al. 2013a, ApJ, 768, L29
Taquet, V., Peters, P. S., Kahane, C., et al. 2013b, A&A, 550, A127
Taquet, V., Bianchi, E., Codella, C., et al. 2019, A&A, 632, A19
Tatematsu, K., Umemoto, T., Kandori, R., & Sekimoto, Y. 2004, ApJ, 606, 333
Thaddeus, P., Kutner, M. L., Penzias, A. A., Wilson, R. W., & Jefferts, K. B. 1972, ApJ, 176, L73
Turner, B. E. 1990, ApJ, 362, L29
Turner, B. E. 2001, ApJS, 136, 579
Ungerechts, H., & Thaddeus, P. 1987, ApJS, 63, 645
van der Tak, F. F. S., Black, J. H., Schöier, F. L., Jansen, D. J., & van Dishoeck, E. F. 2007, A&A, 468, 627
van Dishoeck, E. F., & Blake, G. A. 1998, ARA&A, 36, 317
van Dishoeck, E. F., Blake, G. A., Jansen, D. J., & Groesbeck, T. D. 1995, ApJ, 447, 760
van Dishoeck, E. F., Kristensen, L. E., Mottram, J. C., et al. 2021, A&A, 648, A24
Vastel, C., Phillips, T. G., Ceccarelli, C., & Pearson, J. 2003, ApJ, 593, L97
Vasyunin, A. I., Caselli, P., Dulieu, F., & Jiménez-Serra, I. 2017, ApJ, 842, 33
Vidal, T. H. G., Loison, J.-C., Jaziri, A. Y., et al. 2017, MNRAS, 469, 435
Wakelam, V., Castets, A., Ceccarelli, C., et al. 2004, A&A, 413, 609
Watson, W. D. 1974, ApJ, 188, 35
Wilking, B. A., Meyer, M. R., Greene, T. P., Mikhail, A., & Carlson, G. 2004, AJ, 127, 1131
Wilson, R. W., Jefferts, K. B., & Penzias, A. A. 1970, ApJ, 161, L43
Wu, J., Evans, Neal J., I., Shirley, Y. L., & Knez, C. 2010, ApJS, 188, 313
Yan, Q.-Z., Zhang, B., Xu, Y., et al. 2019, A&A, 624, A6
Yoshida, K., Sakai, N., Nishimura, Y., et al. 2019, PASJ, 71, S18
Zahorecz, S., Jimenez-Serra, I., Testi, L., et al. 2017, A&A, 602, L3
Zahorecz, S., Jimenez-Serra, I., Testi, L., et al. 2021, A&A, 653, A45
Zari, E., Lombardi, M., Alves, J., Lada, C. J., & Bouy, H. 2016, A&A, 587, A106
Zhang, Z.-Y., Gao, Y., Henkel, C., et al. 2014, ApJ, 784, L31
Zhao, B., Caselli, P., Li, Z.-Y., et al. 2016, MNRAS, 460, 2050
Zucker, C., Speagle, J. S., Schlafly, E. F., et al. 2019, ApJ, 879, 125
Zucker, C., Speagle, J. S., Schlafly, E. F., et al. 2020, A&A, 633, A51
Zuckerman, B. 1973, ApJ, 183, 863